

Rapid Outer Radiation Belt Flux Dropouts and Fast Acceleration during the March 2015 and 2013 Storms: Role of ULF Wave Transport from a Dynamic Outer Boundary

Ozeke Louis¹, Mann Ian¹, Dufresne Sydney¹, Olifer Leon¹, Morley Steven², Claudepierre Seth³, Murphy Kyle⁴, Spence Harlan⁵, Baker Daniel⁶, and Degeling Alex⁷

¹University of Alberta

²Los Alamos National Laboratory, Los Alamos, New Mexico, USA

³Space Sciences Department, The Aerospace Corporation, Los Angeles, California, USA

⁴NASA Goddard Spaceflight Center, Code 674, Greenbelt, Maryland, MD 20771, USA

⁵Institute for the Study of Earth, Oceans, and Space, University of New Hampshire, Durham, New Hampshire, USA

⁶Laboratory for Atmospheric and Space Physics, University of Colorado Boulder, Boulder, Colorado, USA

⁷Institute of Space Science, Shandong University, Weihai, China

November 16, 2022

Abstract

We present simulations of the outer radiation belt electron flux during the March 2015 and March 2013 storms using a radial diffusion model. Despite differences in Dst intensity between the two storms the response of the ultra-relativistic electrons in the outer radiation belt was remarkably similar, both showing a sudden drop in the electron flux followed by a rapid enhancement in the outer belt flux to levels over an order of magnitude higher than those observed during the pre-storm interval. Simulations of the ultra-relativistic electron flux during the March 2015 storm show that outward radial diffusion can explain the flux dropout down to $L^*=4$. However, in order to reproduce the observed flux dropout at $L^*<4$ requires the addition of a loss process characterised by an electron lifetime of around one hour operating below $L^*\sim 3.5$ during the flux dropout interval. Nonetheless, during the pre-storm and recovery phase of both storms the radial diffusion simulation reproduces the observed flux dynamics. For the March 2013 storm the flux dropout across all L-shells is reproduced by outward radial diffusion activity alone. However, during the flux enhancement interval at relativistic energies there is evidence of a growing local peak in the electron phase space density at $L^*\sim 3.8$, consistent with local acceleration such as by VLF chorus waves. Overall the simulation results for both storms can accurately reproduce the observed electron flux only when event specific radial diffusion coefficients are used, instead of the empirical diffusion coefficients derived from ULF wave statistics.

**Rapid Outer Radiation Belt Flux Dropouts and Fast Acceleration
during the March 2015 and 2013 Storms: The Role of ULF Wave
Transport from a Dynamic Outer Boundary**

**L. G. Ozeke¹, I. R. Mann¹, S. K. Y. Dufresne¹, L. Olifer¹, S. K. Morley², S. G. Claudepierre^{3,4},
K. R. Murphy⁵, H. E. Spence⁶, D. N. Baker⁷ and A. W. Degeling⁸**

¹Department of Physics, University of Alberta, Edmonton, Alberta, Canada

²Los Alamos National Laboratory, Los Alamos, New Mexico, USA

³Space Sciences Department, The Aerospace Corporation, Los Angeles, California, USA

⁴Department of Atmospheric and Oceanic Sciences, University of California, Los Angeles, CA,
USA

⁵NASA Goddard Spaceflight Center, Code 674, Greenbelt, Maryland, MD 20771, USA

⁶Institute for the Study of Earth, Oceans, and Space, University of New Hampshire, Durham,
New Hampshire, USA

⁷Laboratory for Atmospheric and Space Physics, University of Colorado Boulder, Boulder,
Colorado, USA

⁸Institute of Space Science, Shandong University, Weihai, China

Correspondence to: L. G. Ozeke (lozeke@ualberta.ca)

Key points

The March 2013 outer radiation belt flux dropout is consistent with fast outward ULF wave radial diffusion to a compressed magnetopause

Outward radial diffusion at high L combined with a loss process occurring on $L < 3.5$ are required to explain the March 2015 flux dropout

Event specific radial diffusion coefficients should be used to simulate outer belt flux dynamics especially during the storm main phase

Abstract

We present simulations of the outer radiation belt electron flux during the March 2015 and March 2013 storms using a radial diffusion model. Despite differences in Dst intensity between the two storms the response of the ultra-relativistic electrons in the outer radiation belt was remarkably similar, both showing a sudden drop in the electron flux followed by a rapid enhancement in the outer belt flux to levels over an order of magnitude higher than those observed during the pre-storm interval. Simulations of the ultra-relativistic electron flux during the March 2015 storm show that outward radial diffusion can explain the flux dropout down to $L^*=4$. However, in order to reproduce the observed flux dropout at $L^*<4$ requires the addition of a loss process characterised by an electron lifetime of around one hour operating below $L^*\sim 3.5$ during the flux dropout interval. Nonetheless, during the pre-storm and recovery phase of both storms the radial diffusion simulation reproduces the observed flux dynamics. For the March 2013 storm the flux dropout across all L-shells is reproduced by outward radial diffusion activity alone. However, during the flux enhancement interval at relativistic energies there is evidence of a growing local peak in the electron phase space density at $L^*\sim 3.8$, consistent with local acceleration such as by VLF chorus waves. Overall the simulation results for both storms can accurately reproduce the observed electron flux only when event specific radial diffusion coefficients are used, instead of the empirical diffusion coefficients derived from ULF wave statistics.

1 Introduction

Radial diffusion driven by ultra-low frequency (ULF) waves has long been established as playing a critical role in controlling the acceleration of electrons in the Earth's outer radiation

belt (Fälthammar , 1966 and Schulz & Lanzerotti, 1974). More recently, outward radial diffusion to the magnetopause has also been shown to be an important loss mechanism of outer radiation belt electrons during geomagnetic storms (Loto'aniu et al., 2010, Turner et al., 2012; and Ozeke et al., 2014a). The radial diffusion coefficients, D_{LL} , which determine how quickly the electrons can be transported radially inward and outward, depend on the ULF wave power spectral density of the electric and magnetic fields in space along the electrons drift path (Fei et al., 2006; and Schulz & Lanzerotti, 1974).

Several different approaches have been used to specify the required ULF wave electric and magnetic field power and derive the radial diffusion coefficients. Brautigam and Albert (2000) used a statistical database of ULF wave power spectral density values based on in-situ and ground-based magnetometer measurements to empirically specify the average radial diffusion coefficient resulting from the induced electric field as a function of Kp (see also, Lanzerotti et al., 1973; and Lanzerotti et al., 1978). Using a much larger database of global ground-based magnetometer measurements, as well as in-situ Time History of Events and Macroscale Interactions during Substorms (THEMIS) (Angelopoulos, 2008) and GOES magnetometer (Singer et al., 1996) ULF wave measurements, Ozeke et al. (2014b) also derived analytic expressions for the average electric and magnetic radial diffusion coefficients as a function of Kp. As shown for example by Ozeke et al. (2014a) and Ozeke et al. (2014b), these statistically derived radial diffusion coefficients can produce outer belt electron flux variations in good agreement with observations over long timescales during geomagnetically quiet times. However, for event specific case studies of individual large geomagnetic storms the radial diffusion coefficients derived directly from the measured ULF waves can be significantly different from

those derived from the analytic expressions given in Ozeke et al. (2014b) and Brautigam and Albert (2000), which specify the average D_{LL} value for a given Kp value.

Instead of using the analytic diffusion coefficient based on statistics, an alternate approach to model individual geomagnetic storms is to use a global magnetohydrodynamic (MHD) model to specify the required electric and magnetic fields in space and derive the radial diffusion coefficients from the model ULF wave power spectral density. Z. Li et al. (2017) used this approach to simulate the electron flux in the outer radiation belt during the March 2015 and March 2013 geomagnetic storms, respectively. However, this approach relies on the MHD model accurately reproducing the global spatial distribution and temporal evolution of the electric and magnetic fields as well as their spectral properties, to be able to specify the appropriate radial diffusion coefficients. Huang et al. (2010a,b) showed that the ULF wave radial diffusion transport rates derived using a global MHD model are in general smaller than the transport rates derived directly from observations of the ULF waves.

In this paper we used 63 ground-based magnetometers in North America, Europe and Asia to specify the global distribution of the ULF wave power spectral density (PSD) on the ground during both the March 2015 and March 2013 geomagnetic storms. These D-component magnetic power values are then mapped from the ground to the azimuthal electric field power in space in the magnetic equatorial plane using the approach discussed in Ozeke et al. (2014a, 2014b, see also, Ozeke et al., 2009). These electric field power spectral density values are then used to determine the electric field radial diffusion coefficients.

During the main phase of the March 2015 and March 2013 geomagnetic storms the outer radiation belt electron flux rapidly dropped before subsequently becoming enhanced to levels greater than the pre-storm flux levels, see e.g., Olifer et al. (2018). Here we apply the event specific ULF wave radial diffusion coefficients derived from the ground-based magnetometer measurements to simulate the flux dynamics during the March 2015 and March 2013 geomagnetic storms. In this paper we also examine if the observed initial flux dropout during these storms is consistent with the sole action of outward radial diffusion to a compressed magnetopause driven by enhanced ULF waves.

2 The March 2013 and 2015 Geomagnetic Storms

The March 17 2015 storm was the largest geomagnetic storm of the past 15 years with a minimum Dst value of -223 nT, much lower than the more modest March 17 2013 storm where Dst reached a minimum of -130 nT. Using measurements made by the ACE spacecraft at the L1 Lagrangian point from $\sim 12:30$ UT on March 17 to $04:30$ UT on March 18, Kanekal et al. (2016) present evidence that the March 2015 storm resulted from a Coronal Mass Ejection (CME). The March 17 2013 storm was also caused by a CME and the resulting shock reached the Earth's magnetosphere at $\sim 06:00$ UT (see e.g., Baker et al., 2014b). However, unlike the March 2013 storm the CME on March 2015 was preceded by an interplanetary shock at $04:00$ UT on March 17 which produced a small enhancement in the ultra-relativistic electron flux lasting for approximately two minutes from $04:47$ UT to $04:49$ UT (see, Figure 4 in Kanekal et al., 2016 for details).

The March 2015 and March 2013 geomagnetic storms are both characterized by a sudden increase in the Kp index and the solar wind dynamic pressure on March 17, and at the same time a drop in the Dst index and a strongly negative interplanetary magnetic field Bz, as illustrated in Figure 1. These changes in the solar wind and geomagnetic parameters produce a sudden drop in the magnetopause position and the location of the last closed drift shell (LCDS) on March 17, see Figure 1 panels (i) and (j). Note the LCDS is determined for 90° equatorial pitch angle electrons in the Tsyganenko and Sitnov (2005) magnetic field model using the LANLmax and LANLstar algorithms (Yu et al., 2012) from the LANL* neural network (Morley et al., 2013). However, during the storm time interval on March 17 and 18 the LCDS is obtained from the full calculation at a second adiabatic invariant of $K=0.05 \text{ G}^{1/2}\text{Re}$ using the LANLGeoMag software library (Henderson et al., 2017). The electron flux rapidly decreases at the same time as the sudden drop in the magnetopause position and the location of the LCDS, and then over the course of several subsequent days increases to over an order of magnitude higher than the pre-storm flux. This is shown in the 2.6 MeV energy channel from the Relativistic Electron Proton Telescope (REPT) (Baker et al., 2013) instrument on-board the NASA Van Allen Probes (Spence et al., 2013) in the bottom panels of Figure 1.

High temporal and spatial resolution electron flux measurements taken by the constellation of Global Positioning System (GPS) satellites during these two storms presented in Olifer et al. (2018), show that the timing and extent of the electron flux dropout is closely correlated with the dynamics of the location of the LCDS consistent with the electron flux data in panels (i) and (e) of Figure 1. The local pitch angle (P.A.) distribution of the electrons measured by the two Van Allen Probes during the flux dropout intervals for the March 2015 and March 2013 geomagnetic

storms further validate the close connection of the flux dynamics and the LCDS as presented in Figure 2. Note the pitch angle distributions in Figure 2 are only shown at times where the electron flux is above the instrument noise floor. For the 2015 storm during the dropout interval at times earlier than 23:00 UT on March 17 the flux is too low to fully resolve the pitch angle distribution. Consequently, in Figure 2 only data after 23:00 UT is shown for the March 17, 2015 storm where the flux is high enough to resolve the pitch angle distribution. Figure 2 shows that for both storms at higher L^* values close to the last closed drift shell the pitch angle distribution shows that the lowest flux occurs at pitch angles close to 90° . This is consistent with outward transport to the magnetopause since the higher P.A. particles drift further outwards on the dayside (see e.g., Sibeck et al. 1987). Similar pitch angle distributions during the flux dropout interval of the March 2013 storm are also presented in Baker et al. (2014b). Overall, this suggests the rapid radiation belt losses observed are related to magnetopause shadowing and we investigate this as well as the subsequent fast radiation belt acceleration below.

3 Modeling Methodology

In this paper we simulate the dynamics of the outer radiation belt using a ULF wave driven radial diffusion model, and compare to the dynamics of the outer belt as observed by the Van Allen Probes. The radial diffusion equation expressed in terms of L-shell is given by equation (1)

$$\frac{\partial f}{\partial t} = L^2 \frac{\partial}{\partial L} \left[\frac{D_{LL}}{L^2} \frac{\partial f}{\partial L} \right] - \frac{f}{\tau}. \quad (1)$$

In equation (1) f represents the phase space density of the electrons and it is assumed that the first and second adiabatic invariants, M and J , are conserved (see Schulz & Lanzerotti 1974). The diffusion coefficient and the electron lifetime are represented by D_{LL} and τ respectively.

The solutions to equation (1) only give the electron phase density space density, f . In order to determine the electron flux at fixed energies as a function of L equation (1) is solved for multiple different first adiabatic invariants, M (see e.g., Ozeke et al., 2014a; Ozeke et al., 2014b; and Ozeke et al., 2018, for details).

3.1 Radial Diffusion Coefficients

The radial diffusion coefficient, D_{LL} , is often assumed to be characterized as the sum of the diffusion coefficients due to the uncorrelated azimuthal electric field and the compressional magnetic field perturbations, D_{LL}^E and D_{LL}^B , respectively (see Fei et al., 2006; and Ozeke et al., 2014b). In practice it is difficult to determine if the electric and magnetic perturbations are correlated or uncorrelated, so that there is some uncertainty as to how the D_{LL}^E and D_{LL}^B values should be combined. Here, in order to resolve this uncertainty we neglect the D_{LL}^B term, since in general $D_{LL}^E \gg D_{LL}^B$ (see Ozeke et al., 2014b; and Tu et al., 2012). However, during the storm main phase Pokhotelov et al., 2016 and Olifer et al., 2019 showed that D_{LL}^B may become an order of magnitude greater than D_{LL}^E . Consequently, in order to investigate the impact of D_{LL}^B we have run radial diffusion simulations with and without an added D_{LL}^B term during the storm main phase. Here we assume that the D_{LL}^B term is an order of magnitude greater than D_{LL}^E , consistent with the results presented in Olifer et al. (2019), who showed that at certain L-shells during the main phase of March 2015 storm D_{LL}^B derived from in-situ spacecraft observations of the ULF wave compressional magnetic field can be approximately an order of magnitude greater than D_{LL}^E [E. S.]. Pokhotelov et al. (2016) also showed that during the main phase of the October 2012 storm D_{LL}^B can exceed D_{LL}^E . In a dipole magnetic field, the symmetric radial diffusion coefficients due to the electric field perturbations D_{LL}^E can be expressed as

$$D_{LL}^E = \frac{1}{8B_E^2 R_E^2} L^6 \sum_m P_m^E(m\omega_d) \quad (2)$$

(see, Fei et al., 2006). Here the constants B_E and R_E represent the equatorial magnetic field strength at the surface of the Earth, and the Earth's radius, respectively. In equation (2) the term $P_m^E(m\omega_d)$ represents the power spectral density (PSD) of the electric field perturbations with azimuthal wave-number, m , at wave angular frequency, ω , which satisfy the drift resonance condition given by equation (3)

$$\omega - m\omega_d = 0. \quad (3)$$

Here, ω_d represents the bounce-averaged angular drift frequency of the electron (see Southwood & Kivelson, 1981; and Brizard & Chan, 2001). Since ω_d is a function of the electron's energy and L-shell, in general this introduces an energy and L-shell dependence into the PSD terms $P_m^E(m\omega_d)$ in equation (2). However, the azimuthal electric field PSD obtained observationally from the ground-based magnetometers and mapped to the magnetic equatorial plane shows only a slight dependence on frequency. Here we follow the approach used in Ozeke et al. (2014b) and fit the PSD to a constant so that the resulting D_{LL}^E has no energy dependence.

In addition, as shown in equation (2), D_{LL}^E also depends on the PSD value as a function of the azimuthal wavenumber, m . However, in order to determine the m -value from ground-based magnetometer measurements requires a coherent ULF wave signal at each frequency and L-shell to be detected across a range of longitudinally separated stations (see e.g., Chisham & Mann, 1999) which in general does not occur. In order to resolve the uncertainty in the PSD as a function of m -value, we adopt the approach discussed in Ozeke et al. (2014b) and assume that

221 the magnetometer derived frequency independent equatorial azimuthal electric field PSD, P^{meas} ,
 222 is the sum of the PSD's at each individual m -value, P_m^E , so that

$$P^{meas} = \sum_{m=1}^{\infty} P_m^E \quad (4)$$

223 and the values of the power at each m -value, P_m^E , do not need to be determined to derive the
 224 electric field diffusion coefficient, D_{LL}^E . Note also that only positive wavenumbers satisfy the drift
 225 resonance condition and can contribute to the D_{LL}^E , see equations (2) and (3). Hence, here we also
 226 assume that only half of the measured ULF waves consist of positive m -values. Consequently we
 227 have divided our measured wave amplitudes by a factor of 2 to obtain a value for the azimuthal
 228 electric field PSD, P^{meas} , which only consists of positive ULF wave m -values which contribute
 229 to, D_{LL}^E .

230

231 The approach discussed above gives D_{LL}^E , derived from the measured ULF wave power at each
 232 ground magnetometer station, as a function of dipole L . However, the simulations of the electron
 233 flux are determined in L^* space. In order to convert D_{LL}^E as a function of dipole L to L^* , the L^*
 234 position of the ground magnetometer stations is determined to give D_{LL}^E as a function of L^* at
 235 each time step.

236 3.2 Boundary and Initial Conditions

237 In order to solve the diffusion equation shown in equation (1) the electron phase space density, f ,
 238 must be specified at an inner and outer boundary. For the inner boundary condition, we set
 239 $f(L^*=1)=0$, representing assumed loss to the atmosphere. Here the outer boundary condition is set
 240 at $L^*=5$. At $L^*=5$ the electron phase space density at fixed first and second adiabatic invariants,

M, and ,K, respectively, is derived using the fully relativistic formula presented in Boyd et al. (2014);

$$f = 3.325 \times 10^{-8} \frac{J}{E(E + 2m_o c^2)} \left[\left(\frac{c}{MeVcm} \right)^3 \right]. \quad (5)$$

Here, J is the particle flux at fixed first and second adiabatic invariants in units of $\text{cm}^{-2}\text{sr}^{-1}\text{s}^{-1}\text{keV}^{-1}$, derived using the TS04D magnetic field model (Tsyganenko & Sitnov, 2005), and measurements of the electron flux taken with the Magnetic Electron and Ion Spectrometer (MagEIS) (Blake et al., 2013) and the REPT instruments on-board Van Allen Probes A and B. The particle's kinetic energy and rest mass in MeV are represented by E and $m_o c^2$, respectively (see Boyd et al., 2014 Turner & Li, 2008; and Chen et al., 2005, for more details).

Based on measurements of the electron flux taken by the GPS constellations Olifer et al. (2018) show that for the 2015 storm the relativistic electron flux drops on March 17 at ~08:00 UT and begins to recovery on March 18. Similarly, for the 2013 storm the relativistic electron flux also drops on March 17 at ~08:00 UT but begins to recover slightly early at ~15:00 UT on March 17. The flux dropout as observed by the GPS constellation is also consistent with that observed by the Van Allen Probes. For both storms the flux dropout closely follows the drop in the L^* location of the LCDS (see Olifer et al., 2018 Figure 3 and supporting material Figure S1 in Olifer et al., 2018). In order to investigate whether this observed flux dropout can be reproduced by magnetopause shadowing and outward radial diffusion resulting from the last closed drift shell (LCDS) moving inward to $L^* < 5$, we set the outer boundary condition to zero during the time interval when the LCDS is at $L^* < 5$, this time interval is illustrated in supporting material Figure S2. In addition to the boundary conditions an initial condition must also be specified to solve equation (1). Here we simply set the initial electron phase space density at each first adiabatic

invariant to the observed and initially low electron phase space density, as measured by the Van Allen Probes.

3.3 Electron Loss

The electron lifetimes, τ , in equation (1) are specified using the Orlova et al. (2016) analytic model for the electron lifetimes due to plasmaspheric hiss. Outside the plasmasphere we use the Gu et al. (2012) model to specify the electron lifetimes due to chorus waves. The location of the plasmopause which separates these two loss regimes is determined from March 16 to March 19 for both of the 2013 and 2015 storms using the output from the plasmopause test particle simulation presented Goldstein et al. (2014a, 2014b). During the pre-and post-storm intervals the plasmopause location is determined using the empirical O'Brien and Moldwin (2003) model based on the Dst index. The location of the plasmopause during the March 2015 and March 2013 storms derived using these different models is illustrated in supporting material Figure S3. Similar to the results shown in Mann et al. (2016), our simulations of the ultra-relativistic (>2 MeV) electron flux are only weakly dependent on these electron lifetimes such that, as we show below, the large-scale belt morphology is largely controlled by ULF wave radial diffusion.

4 Results

4.1 Effects of different radial diffusion coefficients

In Figure 3 the ULF wave radial diffusion coefficients derived using different approaches during the March 2015 and 2013 geomagnetic storms are compared. The red and green curves represent the empirically defined radial diffusion coefficients as a function of Kp derived by Brautigam and Albert (2000) for the electromagnetic diffusion term D_{LL}^{EM} [B & A], and by Ozeke et al. (2014b) for the electric diffusion term D_{LL}^E [Ozeke]. The black curves represent the event specific

radial diffusion coefficients derived from the ground-based magnetometer measurements of the ULF waves, D_{LL}^E [E. S.]. In general, there is good overall agreement between these estimates for D_{LL} . However, these results show that D_{LL}^E [E. S.] is usually slightly lower than both D_{LL}^{EM} [B & A] and 2014 D_{LL}^E [Ozeke] except, during short time intervals where D_{LL}^E [E. S.] can be greater than both D_{LL}^{EM} [B & A] and 2014 D_{LL}^E [Ozeke], see panels (e) and (f) in Figure 3.

4.2 Simulations of March 2013 and 2015 storms

Using the approach outlined in the methodology section, including the effects arising from the time dependence of the outer boundary condition, we simulated the relativistic electron flux during the March 2015 and March 2013 storms with our ULF wave radial diffusion model. Figure 4 illustrates the impact of using different diffusion coefficients on the simulated electron flux during the March 2015 and March 2013 storms. Panels (a-b) and (c-d) shown in Figure 4 show the simulated flux derived using empirical expressions for the diffusion coefficients using the specifications from Brautigam and Albert (2000), for D_{LL}^{EM} [B & A] and Ozeke et al. (2014b), for D_{LL}^E [Ozeke], respectively. The simulated electron flux derived using these empirical diffusion coefficients produces flux values which are in general higher than the measured flux; compare for example panels (a-d) with panels (g-h) in Figure 4. However, panels (e) and (f) in Figure 4 also shows that when event-specific radial diffusion coefficients are derived from the ground-based magnetometers measurements of ULF waves, using D_{LL}^E [E. S.], the agreement between the simulated and measured 2.6 MeV energy electron flux during both storms is improved. In order to estimate the possible impact of the compressional magnetic field panels (g) and (h) show simulations with an added D_{LL}^B term during the flux dropout intervals. Here we assume that the D_{LL}^B term is an order of magnitude greater than D_{LL}^E , consistent with the results presented in

Pokhotelov et al., 2016 and Olifer et al., 2019. Note, that simply adding D_{LL}^E and D_{LL}^B may over-
 estimate the rate of diffusion if the electric and magnetic wave fields are correlated, see Fei et al.
 (2016). Panels (g) and (h) show that when the D_{LL}^B is included the flux during the dropout interval
 is reduced down to $L \sim 3.5$, however for both storms there is an increase in the electron flux at
 $L^* < 3$, this increase in the simulated electron flux at $L < 3$ is also illustrated in Figure 5. In Figure
 5 the ratio between the simulated and observed flux is plotted to quantify the level of agreement
 at different L-shells and times. These results clearly illustrate that the empirical diffusion
 coefficients models over-estimate pre-storm and post storm flux on $L \lesssim 3.5$ by over 4 orders of
 magnitude. The agreement between the observed and simulated flux is improved by ~ 2 orders of
 magnitude when the event-specific diffusion coefficients are used, with D_{LL}^E [E. S.] producing a
 slightly better agreement at $L^* < 3$ compared to the simulated flux produced using D_{LL}^{E+B} [E. S.].
 For the remainder of the paper, all electron flux simulations are completed using the event
 specific radial diffusion coefficients, D_{LL}^E [E. S.] derived from ground-based magnetometer
 measurements of ULF waves. In order to better quantify the agreement between the observed
 and simulated flux during the March 2015 and 2013 geomagnetic storms, the flux at fixed $L^* = 4$
 is compared directly in Figure 6. The black and blue curves in Figure 6 illustrate the measured
 and simulated flux, respectively, at energies of 2.1 MeV, 2.6 MeV, 3.4 MeV and 4.2 MeV. In
 general the observed and simulated electron flux results presented in Figure 6 agree to within an
 order of magnitude across all energies and times. However, in general at lower energies the
 simulated electron flux is slightly lower than the observed flux, as illustrated in panels (a) and (b)
 of Figure 6. Conversely, at higher energies the simulated electron flux is in general slightly
 larger than the observed flux, as illustrated in panels (g) and (h) of Figure 6. One possible
 explanation for this slight energy dependent discrepancy between the simulated and observed

electron flux is that the azimuthal electric field ULF wave power used to derive the event specific radial diffusion coefficient, D_{LL}^E [E. S.], has been assumed constant with wave frequency. In general this approximation is reasonable, but during strong geomagnetic storms at $L > 4$ the azimuthal electric field ULF wave power can be slightly higher at lower wave frequencies (see Figure 1 in Ozeke et al. 2014b), which would create slightly greater values for the diffusion coefficients at lower energies than at higher energies. Applying such energy depend radial diffusion coefficients would slightly enhance the simulated flux at lower energies and decrease the simulated flux at higher energies, potentially further improving the agreement between the simulated and observed flux over the range of energies presented in Figure 6.

The model results presented in Figures 4, 5 and 6 clearly show that the observed flux dropout, down to $L^* \gtrsim 4$, is accurately reproduced by our simulations of the March 2015 geomagnetic storm. However, at $L^* \lesssim 4$ during the dropout interval the simulated flux for the March 2015 storm is higher than that which is observed, compare for example panel (e) with panel (i) of Figure 4. Moreover, even increasing D_{LL}^E [E. S.] by an order of magnitude during the flux dropout interval of the March 2015, to account for the potential impact of diffusion due to D_{LL}^B , did not produce enough outward radial transport of the electrons to the magnetopause to reduce the simulated flux below $L^* \lesssim 3.5$ down to the observed flux values, compare panel (g) with panel (i) of Figure 4. Consequently, at $L^* < 4$ during the flux dropout interval there appears to be some evidence for other electron loss processes which may be occurring. Additional loss processes could be active there and scatter electrons into the atmosphere at $L^* < 4$ during the March 2015 storm, such as electron resonance with electro-magnetic ion cyclotron (EMIC) waves (see e.g., Drozdov et al., 2017; Halford et al., 2016; and Ukhorskiy et al., 2010). Alternatively, the

additional loss may also result from resonant wave-particle interactions with small scale size kinetic Alfven waves which are not included in our simulations (see Chaston et al., 2017). Chaston et al. (2017) presented theoretical results indicating that these kinetic Alfven waves may be able to radially diffuse electrons with energies >100 keV outward to the magnetopause, rapidly depleting the outer belt on the timescale of hours during the storm main phase. Nonetheless, the large-scale morphological agreement between the model and the observed flux is in general quite good for the March 2015 event when simulated with D_{LL}^E [E. S.].

For the March 2013 magnetic storm (right column of Figure 4 and Figure 5) there is even better agreement between the simulation results and observations. Significantly, for the March 2013 storm, the simulation results derived using the event-specific radial diffusion coefficient D_{LL}^E [E. S.] is in excellent agreement with the data; results from both the D_{LL}^{EM} [B&A] and D_{LL}^E [Ozeke] empirical models as well as for D_{LL}^{E+B} [E. S.] transporting electrons onto lower L^* values than is observed. Nonetheless, during the main phase of both storms, there appears to be an underestimate of the fast losses at low L^* values which especially for the March 2015 storm, results in penetration of the electron flux to very low L-shell regions, $L^* < 2.8$, for all representations of D_{LL} . This suggests that especially for the March 2015 storm, that the introduction of additional low L^* losses into the 1-dimensional model might improve the agreement with the flux observed by the Van Allen Probes, we investigate this hypothesis below.

4.3 March 2015 Storm: Improved Simulation Incorporating Additional Fast Loss

In order to investigate if the inclusion of an additional loss process can improve the agreement between the simulated and observed flux dynamics of the outer radiation belt we introduce a

377 short period in our simulation during the early storm main phase where we artificially increase
 378 the electron loss. This loss is applied by reducing the electron lifetime τ , to a value shorter than
 379 that resulting from the empirical models for the electron lifetime due to plasmaspheric hiss and
 380 chorus waves included in the simulations presented in the previous section. Specifically, the
 381 electron lifetime τ was set to one hour for lower L^* regions at $L^* < 3.5$ during the observed
 382 dropout intervals, from 08 UT on March 17 to 01 UT on March 18 for the 2015 event, and from
 383 08 UT to 13 UT on March 17 for the 2013 event, see supporting Figure S2. The impact on the
 384 simulated flux of including this short interval of additional fast loss at low L^* values during the
 385 March 2015 geomagnetic storm is illustrated in Figure 7. The panels on the left of Figure 7,
 386 panels (a), (d), (g), and (j), show the flux measured by the Van Allen Probes at energies of 2.1
 387 MeV, 2.6 MeV, 3.4 MeV and 4.2 MeV respectively. Panels (b), (e), (h) and (k) show the
 388 corresponding simulated electron flux, without including any additional artificial fast loss.
 389 Finally, panels (c), (f), (i) and (l) show the corresponding simulated electron flux when the time
 390 interval of 16 hours of fast electron loss characterised by $\tau=1$ hour at $L^* < 3.5$ is included. In both
 391 simulations (middle and right columns in Figure 7) the outer boundary at $L^*=5$ is set to zero
 392 between 08 UT on March 17 to 01 UT on March 18, 2015, matching the time interval when the
 393 last closed drift shell dropped below $L^*=5$, see supporting material Figure S2. Similar results are
 394 also produced when the outer boundary is moved inward to $L^*=4$ during the flux dropout
 395 interval, see supporting material Figure S4. Immediately following the flux dropout interval the
 396 simulated electron flux at $L^* \sim 3.25$ is lower than the observed flux, the difference is greater at the
 397 lower energies than at higher energies. As discussed previously in section 4.2 this energy
 398 dependent difference between the observed and simulated flux could result from the energy
 399 independent radial diffusion used in the simulation. Applying energy dependent diffusion

coefficients slightly increasing the rate of radial diffusion at the lower energies may improve the agreement between observed and simulated electron flux immediately following the flux dropout interval.

The results in Figure 7 clearly indicate that for the March 2015 storm radial transport to the magnetopause, driven by our event specific diffusion coefficients, alone cannot account for the observed electron flux dropout on low L^* values below $L^* \sim 3.5$. However, including an additional artificial fast electron loss at $L^* < 3.5$ characterized by an electron lifetime of one hour during the flux dropout interval from 08 UT to 24 UT on March 17 for the 2015 geomagnetic storm more accurately reproduces the observed flux as illustrated in Figure 7. Nonetheless, the simulation results presented in Figure 7 show that radial diffusion driven by the event specific ULF waves reproduces both the pre-storm flux dynamics before March 17 as well as flux dynamics during the storm recovery interval after March 18. Moreover, recent analysis of the electron phase space density f during the recovery phase of March 2015 geomagnetic storm also shows that the f profiles as a function of L^* are monotonic in L^* and consistent with that produced by inward radial diffusion from $L^* = 5$ driven by ULF waves, see Ozeke et al. (2019).

4.4 March 2013 Storm: Simulation Without Additional Fast Loss

As shown previously in Figures 4 and 5, for the March 2013 storm the flux dropout at an energy of 2.6 MeV is well reproduced by the action of outward radial diffusion to the magnetopause using D_{LL}^E [E. S.]; compare for example panel (f) with panel (h) in Figure 4. Our radial diffusion simulations and observations across a broader range of energies, 2.1 MeV, 2.6 MeV, 3.4 MeV and 4.2 MeV using D_{LL}^E [E. S.], are presented in Figure 8. Figure 8 shows that the observed flux dynamics at these four energies during the March 2013 geomagnetic storm are well-reproduced

by our radial diffusion simulation when driven by the event specific ULF wave radial diffusion coefficients. There is no need to include any additional artificial fast electron loss, which might result from a wave-particle interaction with kinetic Alfvén waves causing loss to the magnetopause (see Chaston et al., 2017), or with EMIC waves causing loss to the atmosphere (see e.g. Drozdov et al., 2017).

In addition, the simulation results shown in Figure 8 are consistent with the results presented by Engebretson et al. (2018), who showed that during the March 2013 storm no EMIC waves were observed either in space or on the ground which were intense enough inside $L < 4$ to account for the observed fast flux dropout. However, statistical studies indicate that EMIC waves can occur over a narrow range of L-shells and local times making detection of the waves difficult (see e.g., Usanova et al., 2012; and Saikin et al., 2015). Consequently, it is possible that spatially limited intense EMIC waves occurred during the March 2013 storm on low L-shells but no instruments were present at the exact location of the waves to detect their presence. Moreover, EMIC waves may not be able to account for the flux dropout observed over a wide range of L-shells if waves only occurred over a narrow range of L-shells. ULF wave transport from $L^* = 5$ appears to be able to largely reproduce the observed characteristics of the radiation belt. Nonetheless, during the flux enhancement interval after March 18, 2013, the observed flux at $L^* \sim 3.5$ is still slightly more intense than the simulated flux (see Figure 8).

Previous studies of the March 2013 geomagnetic storm have suggested that local acceleration of the outer radiation belt electrons by resonance with chorus waves could have contributed to the flux enhancement during the recovery phase on March 18 and 19 (see e.g., Z. Li et al. 2014; W.

Li et al. 2014; Ma et al. 2018; Foster et al. 2014; and Boyd et al., 2014). To investigate the possible role for local acceleration in the March 2013 storm we also examine the profiles of electron phase space density as a function of L^* . The occurrence of growing local peaks in the electron phase space density is commonly used to identify regions where a local acceleration mechanism could be active (see e.g., Reeves et al., 2013). Conversely, the absence of growing local peaks could indicate that the inward radial diffusion mechanism may be responsible for the electron acceleration (see e.g., Ozeke et al., 2019). However, as discussed by Green and Kivelson (2004), and more recently by Loridan et al. (2019), inaccuracy in the magnetic field model can result in artificial growing peaks being produced in the electron phase space density profile, or alternatively cause growing peaks to be removed. Consequently, here we examine both the evolution of the electron phase space density profiles as well as comparing the simulated and observed electron flux to determine which acceleration mechanisms may be responsible for the outer radiation belt flux enhancement during the March 2013 storm.

The results presented in Figure 9 show the evolution of the electron phase space density, f , as a function of L^* at a fixed first adiabatic invariant of $M=2750$ MeV/G and fixed second adiabatic invariant of $K=0.17$ G^{1/2}Re, during the main phase of the March 2013 storm and the subsequent recovery phase. In addition, similar electron phase space density profiles at lower, $M=1590$ MeV/G, and higher, $M=3980$ MeV/G, first adiabatic invariants are also presented in the supporting material in Figure S5 and S6, respectively. These f values as a function of L^* are derived using the TS04D magnetic field model and use electron flux measurements taken with both the MagEIS and the REPT instruments using the approach outlined in Morley et al. (2013) and Schiller et al. (2017). The phase space density data for the March 2013 event is publicly

available from <https://drive.google.com/drive/u/0/folders/0ByNhSbWkAgdfaGt6TnJMcElhUTg>.

As mentioned in the acknowledgement this is the data repository for the Geospace Environment Modeling (GEM) challenge events in 2013 selected by the *Quantitative Assessment of Radiation Belt Modeling* focus group.

The phase space density profiles presented in Figure 9 do show a locally growing peak in f at $L^* \sim 3.8$, see panels (i-l) in Figure 9, consistent with the action of local acceleration of the electrons by chorus waves. However, at higher L^* values above $L^* = 4$, the f profiles continuously increase with L^* reaching values higher than those which occur at the locally growing peak near $L^* = 3.8$, consistent with inward radial diffusion of the electrons from a source at or beyond the outer boundary. Consequently, it is possible that the outer radiation belt flux dynamics at ultra-relativistic energies (> 2 MeV) during the period of enhancement for the March 2013 storm are caused by the action of inward radial diffusion of electrons and from the action of local acceleration by chorus waves at $L^* \sim 3.8$. The absence of any local acceleration processes in the simulation results presented in Figure 8 would explain why the simulated flux is slightly lower than that which is observed at $L^* \sim 3.8$, see Figure 8.

The electron phase space density profiles derived in Boyd et al. (2014), Ma et al. (2018) and W. Li et al. (2014) also indicate that locally growing peaks occurred near $L^* = 3.8$ between ~ 10 UT on March 17 and ~ 05 UT on March 18, consistent with our phase space density profiles presented in Figures 9 (a) to (d) (see also supporting material in panels (a) to (d) of Figures S5 and S6). In addition, Foster et al. (2014) also show that an enhancement in the chorus wave intensity near $L^* \sim 4$ also occurred on March 17 supporting the hypothesis that these locally

growing peaks are due to acceleration by chorus waves. The results presented in Ma et al. (2018), W. Li et al. (2014) and in our Figure 9 (see also Figures S5 and S6 in the supporting material) indicate that the local electron phase space density peak at $L^* \sim 3.8$ does not continue to grow at times later than ~ 05 UT on March 18. However, our results indicate that at times after ~ 05 UT on March 18 the electron phase space density further increases across all L-shells greater than $L^* \sim 4$. Moreover, these subsequent increases in the electron phase space density beyond $L^* \sim 4$ become progressively greater with increasing L-shell, so that no locally growing peaks occur at $L^* \gtrsim 4$, see Figure 9 panels (e) to (l) (also see the same panels in Figure S5 and S6 in the supporting material). Consequently, this additional enhancement in the electron phase density at times after ~ 05 UT on March 18 is not consistent with the occurrence of growing peaks associated with local acceleration of the electrons inside the apogee of the Van Allen Probes, since the phase space density profile monotonically increases with increasing L^* , beyond $L^* \sim 4$.

However, the additional enhancement in the electron phase space density beyond $L^* \sim 4$ could result from a local acceleration mechanism occurring at L^* values higher than the apogee of the Van Allen Probes (see Boyd et al., 2018). Alternatively, the enhancement could result from the inward radial transport of energetic electrons from a plasmasheet source. In order to resolve which process may be responsible for the increase in the electron flux beyond $L^* \sim 4$ and during times after ~ 05 UT on March 18 would require additional measurements of the electron phase space density beyond the apogee of the Van Allen Probes. Nonetheless, our simulations results presented in Figure 8 clearly indicate that inward transport of the electrons from $L^* = 5$ driven by the event specific ULF wave radial diffusion coefficients can accurately reproduce the observed

electron flux dynamics during the March 2013 storm, particularly on the higher L-shells beyond the location of the growing phase space density peak.

5 Discussion and Conclusions

In this paper we used a one-dimensional ULF wave radial diffusion model driven by global ground-based magnetometer measurements to simulate the dynamics and acceleration of equatorially mirroring ultra-relativistic electrons during the intense March 2015, and the less intense March 2013, magnetic storm. Despite the difference in storm intensity in terms of Dst and in solar wind parameters between the two March 2015 and March 2013 storms we show that the hour to day timescale response of the ultra-relativistic electrons in the outer radiation belt was remarkably similar. Both events show a self-similar sudden drop in the electron flux followed by a rapid enhancement in the outer belt flux to levels over an order of magnitude higher than those observed during the pre-storm interval. In addition, for both the March 2015 and 2013 storms the measured electron flux dropout occurred at ~08 UT on March 17, see Olifer et al. (2018).

During the flux dropout interval, the last closed drift shell (LCDS) moved inward to $L^* \sim 5$ and butterfly pitch-angle distributions with a minimum flux near 90° for both storms were observed near the apogee of the Van Allen Probes, consistent with the hypothesis that the flux dropout resulted from magnetopause shadowing and outward ULF wave driven radial diffusion. Turner et al. (2014) also reached a similar conclusion in their analysis of a flux dropout event which occurred in September 2012. In our simulation results, the flux at the outer boundary, defined to be at $L^* = 5$, was set to zero during this dropout interval, consistent with magnetopause

shadowing, since the measured flux was either at the noise floor of instrument or the probes did not reach $L^*=5$ during the dropout interval (see Figure 1 and Figure 2 as well as supporting material Figure S2). Note that changing the time extent of the dropout interval where the flux at $L^*=5$ was set to zero by ± 2 hours did not significantly affect the simulation results.

5.1 March 2015 Storm

Radial diffusion simulations of the March 2015 storm showed that outward radial diffusion and magnetopause shadowing could together almost completely explain the observed losses and short-lived flux dropout down to $L^*\sim 4$, as well as the subsequent electron flux recovery and enhancement. However, at $L^*<4$ the simulated flux was greater than that which was observed suggesting a missing loss process at low L . We show that by including an additional temporally limited period of enhanced artificial loss characterized by an electron lifetime of one hour restricted to $L^*<3.5$, the observed flux dropout at $L^*<4$ can be successfully reproduced by our simulation. This additional loss process could result from the resonant wave-particle interaction with EMIC waves causing extra low L^* loss due to pitch-angle scattering the electrons into the atmosphere. In support of this hypothesis Runov et al., (2016) show that EMIC waves were observed by the THEMIS E satellite during the 17 March 2015 storm, which were not detected during the pre-storm interval. Alternatively, the additional loss could also result from the resonant wave-particle interaction with small scale kinetic Alfvén waves causing enhanced outward diffusion to the magnetopause depleting the electron flux on the lower L-shells (Chaston et al. 2017). Nonetheless, overall during both the pre-storm and recovery phases the large-scale morphology and dynamics of the outer radiation belt flux at ultra-relativistic energies are well-reproduced using the radial diffusion model when driven by event-specific radial diffusion coefficients constrained by the global ULF waves observed by ground-based magnetometers.

561

562 5.2 March 2013 Storm

563 For the March 2013 storm, the flux dropout across all L-shells is well reproduced by the radial
564 diffusion simulation alone. This indicates that for this storm outward radial diffusion to the
565 magnetopause acting alone can explain the observed flux drop across all L-shells without the
566 need for any other additional loss processes. These radial diffusion simulations of the flux
567 dropout during the March 2013 storm are also consistent with the test particle simulations
568 presented in Sorathia et al. (2018). In addition, the steady inward motion of the observed outer
569 radiation belt flux during the pre-storm interval, before March 17, is also remarkably well-
570 reproduced by our radial diffusion simulation. However, during the initial flux recovery interval
571 on March 18 the simulated flux near $L^* \sim 3.8$ is somewhat lower than that which is observed.

572

573 Previous studies have indicated that the flux enhancement during the March 2013 storm could
574 have been related to local acceleration, such as that due to chorus waves (see Z. Li et al., 2014;
575 W. Li et al., 2014; Ma et al., 2018; and Boyd et al., 2014). Boyd et al. (2014) presented evidence
576 of a growing local peak in the electron phase space density, f , at $L^* \sim 4$, consistent with local
577 acceleration by chorus waves. Similarly, W. Li et al. (2014) and Ma et al. (2018) also presented
578 evidence of a growing local peak in f as a function of L^* and also simulated the initial flux
579 recovery interval using a diffusion model included the effects of local acceleration by chorus
580 waves as well as acceleration arising from radial diffusion by ULF waves. The profiles of f as a
581 function of L^* presented in Boyd et al. (2014), W. Li et al. (2014), Ma et al. (2018) and Z. Li et
582 al. (2014) all show that the highest values of the electron phase space density occurred near
583 $L^* \sim 4$, the location of a locally growing peak in f , suggesting that local acceleration was the

dominant acceleration mechanism. The profiles in f , presented here for the March 2013 storm also show a growing peak near $L^* \sim 3.8$ immediately following the flux dropout interval. However, at later times and at higher L^* values beyond $L^* = 4$ the values of the electron phase space density gradually become greater than those at the location of the local peak in the f profile (see our Figure 9). Our results therefore indicate that during this storm that inward radial diffusion by ULF may have played a significant role in the acceleration and flux recovery at $L^* \gtrsim 4$. However local acceleration may also have played an important role in the electron flux dynamics during the initial flux recovery interval on lower L-shells near $L^* \sim 3.8$.

For both the March 2015 and March 2013 storms the simulation results presented in this paper demonstrate that the large-scale morphology and dynamics of the outer electron radiation belt can be successfully modeled with ULF wave radial diffusion. The results further highlight the importance of using radial diffusion coefficients derived from event specific ULF wave measurements, instead of using empirical models for D_{LL} based on ULF wave statistics, in order to accurately simulate the overall flux dynamics in the outer radiation belt.

607
608
609
610
611
612
613
614
615
616
617
618
619
620
621
622
623
624
625
626
627
628
629

630

631 **6 References**

632

633 Angelopoulos, V. (2008), The THEMIS Mission, *Space Sci. Rev.*, 141(1-4), 5-34, doi:

634 10.1007/s11214-008-9336-1.

635 Baker, D. N. et al. (2014a), An impenetrable barrier to ultrarelativistic electrons in the Van Allen

636 radiation belts, *Nature*, 515, 531, doi: 10.1038/nature13956.

637 Baker, D. N. et al. (2014b), Gradual diffusion and punctuated phase space density

638 enhancements of highly relativistic electrons: Van Allen Probes observations, *Geophys.*

639 *Res. Lett.*, 41(5), 1351-1358, doi: 10.1002/2013GL058942.

640 Baker, D. N. et al. (2013), The Relativistic Electron-Proton Telescope (REPT) Instrument on

641 Board the Radiation Belt Storm Probes (RBSP) Spacecraft: Characterization of Earth's

642 Radiation Belt High-Energy Particle Populations, *Space Science Reviews*, 179(1), 337-

643 381, doi: 10.1007/s11214-012-9950-9.

644 Baker, D. N. et al. (2016), Highly relativistic radiation belt electron acceleration, transport, and

645 loss: Large solar storm events of March and June 2015, *Journal of Geophysical*

646 *Research: Space Physics*, 121(7), 6647-6660, doi: 10.1002/2016JA022502.

647 Blake, J. B., P. A. Carranza, S. G. Claudepierre, J. H. Clemmons, W. R. Crain, Y. Dotan, J. F.

648 Fennell, F. H. Fuentes, R. M. Galvan, and J. S. George (2013), The magnetic electron

649 ion spectrometer (MagEIS) instruments aboard the radiation belt storm probes (RBSP)

650 spacecraft, *Space Science Reviews*, 179, 383-421.

651 Boyd, A. J., D. L. Turner, G. D. Reeves, H. E. Spence, D. N. Baker, and J. B. Blake (2018),

652 What Causes Radiation Belt Enhancements: A Survey of the Van Allen Probes Era,

653 *Geophys. Res. Lett.*, 45(11), 5253-5259, doi: 10.1029/2018GL077699.

654 Boyd, A. J., H. E. Spence, S. G. Claudepierre, J. F. Fennell, J. B. Blake, D. N. Baker, G. D.
 655 Reeves, and D. L. Turner (2014), Quantifying the radiation belt seed population in the 17
 656 March 2013 electron acceleration event, *Geophysical Research Letters*, *41*(7), 2275-
 657 2281, doi: 10.1002/2014GL059626.

658 Brautigam, D. H., G. P. Ginet, J. M. Albert, J. R. Wygant, D. E. Rowland, A. Ling, and J. Bass
 659 (2005), CRRES electric field power spectra and radial diffusion coefficients, *J. Geophys.*
 660 *Res.*, *110*, doi: 10.1029/2004JA010612.

661 Brizard, A. J. and A. A. Chan (2001), Relativistic bounce-averaged quasilinear diffusion
 662 equation for low-frequency electromagnetic fluctuations, *Phys Plasmas*, *8*(11), 4762-
 663 4771, doi: 10.1063/1.1408623.

664 Carpenter, D. L. and R. R. Anderson (1992), An ISEE/whistler model of equatorial electron
 665 density in the magnetosphere, *J. Geophys. Res.*, *97*, 1097-1108, doi:
 666 10.1029/91JA01548.

667 Chaston, C. C., J. W. Bonnell, J. R. Wygant, G. D. Reeves, D. N. Baker, D. B. Melrose, and I. H.
 668 Cairns (2017), Radial transport of radiation belt electrons in kinetic field-line resonances,
 669 *Geophys. Res. Lett.*, *44*(16), 8140-8148, doi: 10.1002/2017GL074587.

670 Chen, Y., R. H. W. Friedel, G. D. Reeves, T. G. Onsager, and M. F. Thomsen (2005),
 671 Multisatellite determination of the relativistic electron phase space density at
 672 geosynchronous orbit: Methodology and results during geomagnetically quiet times, *J.*
 673 *Geophys. Res.*, *110*, doi: 10.1029/2004JA010895.

674 Chisham, G. and I. R. Mann (1999), A Pc5 ULF wave with large azimuthal wavenumber
 675 observed within the morning sector plasmasphere by Sub-Auroral Magnetometer
 676 Network, *J. Geophys. Res.*, *104*, 14717-14727, doi: 10.1029/1999JA900147.

677 Drozdov, A. Y., Y. Y. Shprits, M. E. Usanova, N. A. Aseev, A. C. Kellerman, and H. Zhu (2017),
 678 EMIC wave parameterization in the long-term VERB code simulation, *J. Geophys. Res.*
 679 *Space Physics*, 122(8), 8488-8501, doi: 10.1002/2017JA024389.

680 Drozdov, A. Y., Y. Y. Shprits, K. G. Orlova, A. C. Kellerman, D. A. Subbotin, D. N. Baker, H. E.
 681 Spence, and G. D. Reeves (2015), Energetic, relativistic, and ultrarelativistic electrons:
 682 Comparison of long-term VERB code simulations with Van Allen Probes measurements,
 683 *J. Geophys. Res. Space Physics*, 120(5), 3574-3587, doi: 10.1002/2014JA020637.

684 Engebretson, M. J. et al. (2018), EMIC wave events during the four GEM QARBM challenge
 685 intervals, *J. Geophys. Res. Space Physics*, 0, doi: 10.1029/2018JA025505.

686 Fei, Y., A. A. Chan, S. R. Elkington, and M. J. Wiltberger (2006), Radial diffusion and MHD
 687 particle simulations of relativistic electron transport by ULF waves in the September
 688 1998 storm, *J. Geophys. Res.*, 111, doi: 10.1029/2005JA011211.

689 Foster, J. C. et al. (2014), Prompt energization of relativistic and highly relativistic electrons
 690 during a substorm interval: Van Allen Probes observations, *Geophys. Res. Lett.*, 41(1),
 691 20-25, doi: 10.1002/2013GL058438.

692 Goldstein, J., S. D. Pascuale, C. Kletzing, W. Kurth, K. J. Genestreti, R. M. Skoug, B. A. Larsen,
 693 L. M. Kistler, C. Mouikis, and H. Spence (2014a), Simulation of Van Allen Probes
 694 plasmopause encounters, *J. Geophys. Res. Space Physics*, 119(9), 7464-7484, doi:
 695 10.1002/2014JA020252.

696 Goldstein, J., M. F. Thomsen, and A. DeJong (2014b), In situ signatures of residual
 697 plasmaspheric plumes: Observations and simulation, *J. Geophys. Res. Space Physics*,
 698 119(6), 4706-4722, doi: 10.1002/2014JA019953. Gu, X., Y. Y. Shprits, and B. Ni (2012),
 699 Correction to "Parameterized lifetime of radiation belt electrons interacting with lower-
 700 band and upper-band oblique chorus wave", *Geophysical Research Letters*, 39(17), n/a,
 701 doi: 10.1029/2012GL053568.

Halford, A. J., B. J. Fraser, S. K. Morley, S. R. Elkington, and A. A. Chan (2016), Dependence of EMIC wave parameters during quiet, geomagnetic storm, and geomagnetic storm phase times, *J. Geophys. Res. Space Physics*, *121*(7), 6277-6291, doi: 10.1002/2016JA022694.

Henderson, M., Morley, S., Niehof, J., & Larsen, B. (2017). drsteve/LANLGeoMag: LANLGeoMag v.1.5.15-alpha. <https://doi.org/10.5281/zenodo.1133782>

Huang, C., H. E. Spence, M. K. Hudson, and S. R. Elkington (2010a), Modeling radiation belt radial diffusion in ULF wave fields: 2. Estimating rates of radial diffusion using combined MHD and particle codes, *J. Geophys. Res.*, *115*, doi: 10.1029/2009JA014918.

Huang, C., H. E. Spence, H. J. Singer, and W. J. Hughes (2010b), Modeling radiation belt radial diffusion in ULF wave fields: 1. Quantifying ULF wave power at geosynchronous orbit in observations and in global MHD model, *J. Geophys. Res.*, *115*, doi: 10.1029/2009JA014917.

Kanekal, S. G. et al. (2016), Prompt acceleration of magnetospheric electrons to ultrarelativistic energies by the 17 March 2015 interplanetary shock, *J. Geophys. Res. Space Physics*, *121*(8), 7622-7635, doi: 10.1002/2016JA022596.

Lanzerotti, L. J. and C. G. Morgan (1973), ULF geomagnetic power near L = 4: 2. Temporal variation of the radial diffusion coefficient for relativistic electrons, *J. Geophys. Res.*, *78*(22), 4600-4610, doi: 10.1029/JA078i022p04600.

Lanzerotti, L. J., D. C. Webb, and C. W. Arthur (1978), Geomagnetic field fluctuations at synchronous orbit 2. Radial diffusion, *J. Geophys. Res.*, *83*, 3866-3870, doi: 10.1029/JA083iA08p03866.

Li, W. et al. (2016), Radiation belt electron acceleration during the 17 March 2015 geomagnetic storm: Observations and simulations, *J. Geophys. Res. Space Physics*, *121*(6), 5520-5536, doi: 10.1002/2016JA022400.

727 Li, W. et al. (2014), Radiation belt electron acceleration by chorus waves during the 17 March
 728 2013 storm, *J. Geophys. Res. Space Physics*, 119(6), 4681-4693, doi:
 729 10.1002/2014JA019945.

730 Li, Z., M. Hudson, A. Jaynes, A. Boyd, D. Malaspina, S. Thaller, J. Wygant, and M. Henderson
 731 (2014), Modeling gradual diffusion changes in radiation belt electron phase space
 732 density for the March 2013 Van Allen Probes case study, *J. Geophys. Res. Space*
 733 *Physics*, 119(10), 8396-8403, doi: 10.1002/2014JA020359.

734 Li, Z., M. Hudson, J. Paral, M. Wiltberger, and D. Turner (2016), Global ULF wave analysis of
 735 radial diffusion coefficients using a global MHD model for the 17 March 2015 storm,
 736 *Journal of Geophysical Research: Space Physics*, 121(7), 6196-6206, doi:
 737 10.1002/2016JA022508.

738 Li, Z., M. Hudson, M. Patel, M. Wiltberger, A. Boyd, and D. Turner (2017), ULF wave analysis
 739 and radial diffusion calculation using a global MHD model for the 17 March 2013 and
 740 2015 storms, *J. Geophys. Res. Space Physics*, 122(7), 7353-7363, doi:
 741 10.1002/2016JA023846.

742 Loridan, V., J. Ripoll, W. Tu, and G. S. Cunningham (2019), On the use of different magnetic
 743 field models for simulating the dynamics of the outer radiation belt electrons during the
 744 October 1990 storm, *J. Geophys. Res. Space Physics*, 0, doi: 10.1029/2018JA026392.

745 Ma, Q. et al. (2018), Quantitative Evaluation of Radial Diffusion and Local Acceleration
 746 Processes During GEM Challenge Events, *J. Geophys. Res. Space Physics*, 123(3),
 747 1938-1952, doi: 10.1002/2017JA025114.

748 Mann, I. R. et al. (2016), Explaining the dynamics of the ultra-relativistic third Van Allen radiation
 749 belt, *Nature Physics*, 12, 978, doi: 10.1038/nphys3799.

750 Morley, S. K., Koller, J., Welling, D. T., Larsen, B. A., Henderson, M. G., & Niehof, J. T. (2011).
 751 Spacepy—A python-based library of tools for the space sciences. In Proceedings of the
 752 9th Python in science conference (SciPy 2010) (pp. 39–45). Austin, TX.
 753 Morley, S. K., M. G. Henderson, G. D. Reeves, W. F. R. H., and D. N. Baker (2013), Phase
 754 Space Density matching of relativistic electrons using the Van Allen Probes: REPT
 755 results, *Geophys. Res. Lett.*, *40*(18), 4798-4802, doi: 10.1002/grl.50909.
 756 O'Brien, T. P. and M. B. Moldwin (2003), Empirical plasmopause models from magnetic indices,
 757 *Geophys. Res. Lett.*, *30*(4), doi: 10.1029/2002GL016007.
 758 Olifer, L., I. R. Mann, S. K. Morley, L. G. Ozeke, and D. Choi (2018), On the Role of Last Closed
 759 Drift Shell Dynamics in Driving Fast Losses and Van Allen Radiation Belt Extinction, *J.*
 760 *Geophys. Res. Space Physics*, *123*(5), 3692-3703, doi: 10.1029/2018JA025190.
 761 Olifer, L., I. R. Mann, L. G. Ozeke, I. J. Rae, and S. K. Morley (2019), On the Relative Strength
 762 of Electric and Magnetic ULF Wave Radial Diffusion During the March 2015
 763 Geomagnetic Storm, *J. Geophys. Res. Space Physics*, *124*(4), 2569-2587, doi:
 764 10.1029/2018JA026348.
 765 Orlova, K., Y. Shprits, and M. Spasojevic (2016), New global loss model of energetic and
 766 relativistic electrons based on Van Allen Probes measurements, *J. Geophys. Res.*
 767 *Space Physics*, *121*(2), 1308-1314, doi: 10.1002/2015JA021878.
 768 Ozeke, L. G., I. R. Mann, and I. J. Rae (2009), Mapping guided Alfvén wave magnetic field
 769 amplitudes observed on the ground to equatorial electric field amplitudes in space, *J.*
 770 *Geophys. Res.*, *114*, doi: 10.1029/2008JA013041.
 771 Ozeke, L. G., I. R. Mann, S. G. Claudepierre, M. Henderson, S. K. Morley, K. R. Murphy, L.
 772 Olifer, H. E. Spence, and D. N. Baker (2019), The March 2015 Superstorm Revisited:
 773 Phase Space Density Profiles and Fast ULF Wave Diffusive Transport, *J. Geophys. Res.*
 774 *Space Physics*, *124*(2), 1143-1156, doi: 10.1029/2018JA026326.

775 Ozeke, L. G., I. R. Mann, K. R. Murphy, A. W. Degeling, S. G. Claudepierre, and H. E. Spence
 776 (2018), Explaining the apparent impenetrable barrier to ultra-relativistic electrons in the
 777 outer Van Allen belt, *Nature Communications*, 9(1), 1844, doi: 10.1038/s41467-018-
 778 04162-3.

779 Ozeke, L. G., I. R. Mann, D. L. Turner, K. R. Murphy, A. W. Degeling, I. J. Rae, and D. K. Milling
 780 (2014a), Modeling cross L shell impacts of magnetopause shadowing and ULF wave
 781 radial diffusion in the Van Allen belts, *Geophys. Res. Lett.*, 41(19), 6556-6562, doi:
 782 10.1002/2014GL060787.

783 Ozeke, L. G., I. R. Mann, K. R. Murphy, I. Jonathan Rae, and D. K. Milling (2014b), Analytic
 784 expressions for ULF wave radiation belt radial diffusion coefficients, *Journal of*
 785 *Geophysical Research: Space Physics*, 119(3), 1587-1605, doi:
 786 10.1002/2013JA019204.

787 Pokhotelov, D., I. J. Rae, K. R. Murphy, I. R. Mann, and L. Ozeke (2016), Effects of ULF wave
 788 power on relativistic radiation belt electrons: 8–9 October 2012 geomagnetic storm, *J.*
 789 *Geophys. Res. Space Physics*, 121(12), 11,779, doi: 10.1002/2016JA023130.

790 Reeves, G. D. et al. (2013), Electron Acceleration in the Heart of the Van Allen Radiation Belts,
 791 *Science*, 341(6149), 991, doi: 10.1126/science.1237743.

792 Runov, A., Zhang, X. J., and Angelopoulos, V. (2016), Evolution of partial ring current ion pitch
 793 angle distributions during the main phase of a storm on 17 March 2015, *J. Geophys.*
 794 *Res. Space Physics*, 121, 5284– 5293, doi:10.1002/2016JA022391.

795 Saikin, A. A., J. -. Zhang, R. C. Allen, C. W. Smith, L. M. Kistler, H. E. Spence, R. B. Torbert, C.
 796 A. Kletzing, and V. K. Jordanova (2015), The occurrence and wave properties of H+-,
 797 He+-, and O+-band EMIC waves observed by the Van Allen Probes, *J. Geophys. Res.*
 798 *Space Physics*, 120(9), 7477-7492, doi: 10.1002/2015JA021358.

799 Schiller, Q., W. Tu, A. F. Ali, X. Li, H. C. Godinez, D. L. Turner, S. K. Morley, and M. G.
 800 Henderson (2017), Simultaneous event-specific estimates of transport, loss, and source
 801 rates for relativistic outer radiation belt electrons, *J. Geophys. Res. Space Physics*,
 802 122(3), 3354-3373, doi: 10.1002/2016JA023093.

803 Schulz, M. and L. J. Lanzerotti (1974), *Particle Diffusion in the Radiation Belts*, vol. 7, Physics
 804 and Chemistry in Space 7 ed., 215 pp., Springer-Verlag, New York Heidelberg Berlin.

805 Shue, J.-H. et al. (1998), Magnetopause location under extreme solar wind conditions, *J.*
 806 *Geophys. Res.*, 103, 17691-17700, doi: 10.1029/98JA01103.

807 Sibeck, D. G., R. W. McEntire, A. T. Y. Lui, R. E. Lopez, and S. M. Krimigis (1987), Magnetic
 808 field drift shell splitting: Cause of unusual dayside particle pitch angle distributions during
 809 storms and substorms, *J. Geophys. Res.*, 92, 13485-13497, doi:
 810 10.1029/JA092iA12p13485.

811 Singer, H., L. Matheson, R. Grubb, A. Newman, and D. Bouwer (1996), Monitoring space
 812 weather with the GOES magnetometers, *GOES-8 and Beyond* E. R. Washwell, Proc. SPIE
 813 Int. Soc. Opt. Eng., 2812, 299–308.

814 Sorathia, K. A., A. Y. Ukhorskiy, V. G. Merkin, J. F. Fennell, and S. G. Claudepierre (2018),
 815 Modeling the Depletion and Recovery of the Outer Radiation Belt During a Geomagnetic
 816 Storm: Combined MHD and Test Particle Simulations, *J. Geophys. Res. Space Physics*,
 817 123(7), 5590-5609, doi: 10.1029/2018JA025506.

818 Southwood, D. J. and M. G. Kivelson (1981), Charged particle behavior in low-frequency
 819 geomagnetic pulsations 1. Transverse waves, *J. Geophys. Res.*, 86, 5643-5655, doi:
 820 10.1029/JA086iA07p05643.

821 Spence, H. E. et al. (2013), Science Goals and Overview of the Radiation Belt Storm Probes
 822 (RBSP) Energetic Particle, Composition, and Thermal Plasma (ECT) Suite on NASA's

823 Van Allen Probes Mission, *Space Science Reviews*, 179(1), 311-336, doi:
824 10.1007/s11214-013-0007-5.

825 Tsyganenko, N. A. and M. I. Sitnov (2005), Modeling the dynamics of the inner magnetosphere
826 during strong geomagnetic storms, *J. Geophys. Res.*, 110, doi: 10.1029/2004JA010798.

827 Tu, W., S. R. Elkington, X. Li, W. Liu, and J. Bonnell (2012), Quantifying radial diffusion
828 coefficients of radiation belt electrons based on global MHD simulation and spacecraft
829 measurements, *J. Geophys. Res.*, 117, doi: 10.1029/2012JA017901.

830 Turner, D. L. et al. (2014), On the cause and extent of outer radiation belt losses during the 30
831 September 2012 dropout event, *J. Geophys. Res. Space Physics*, 119(3), 1530-1540,
832 doi: 10.1002/2013JA019446.

833 Turner, D. L. and X. Li (2008), Radial gradients of phase space density of the outer radiation
834 belt electrons prior to sudden solar wind pressure enhancements, *Geophys. Res. Lett.*,
835 35(18), doi: 10.1029/2008GL034866.

836 Ukhorskiy, A. Y., Y. Y. Shprits, B. J. Anderson, K. Takahashi, and R. M. Thorne (2010), Rapid
837 scattering of radiation belt electrons by storm-time EMIC waves, *Geophys. Res. Lett.*,
838 37(9), doi: 10.1029/2010GL042906.

839 Usanova, M. E., I. R. Mann, J. Bortnik, L. Shao, and V. Angelopoulos (2012), THEMIS
840 observations of electromagnetic ion cyclotron wave occurrence: Dependence on AE,
841 SYMH, and solar wind dynamic pressure, *J. Geophys. Res.*, 117, doi:
842 10.1029/2012JA018049.

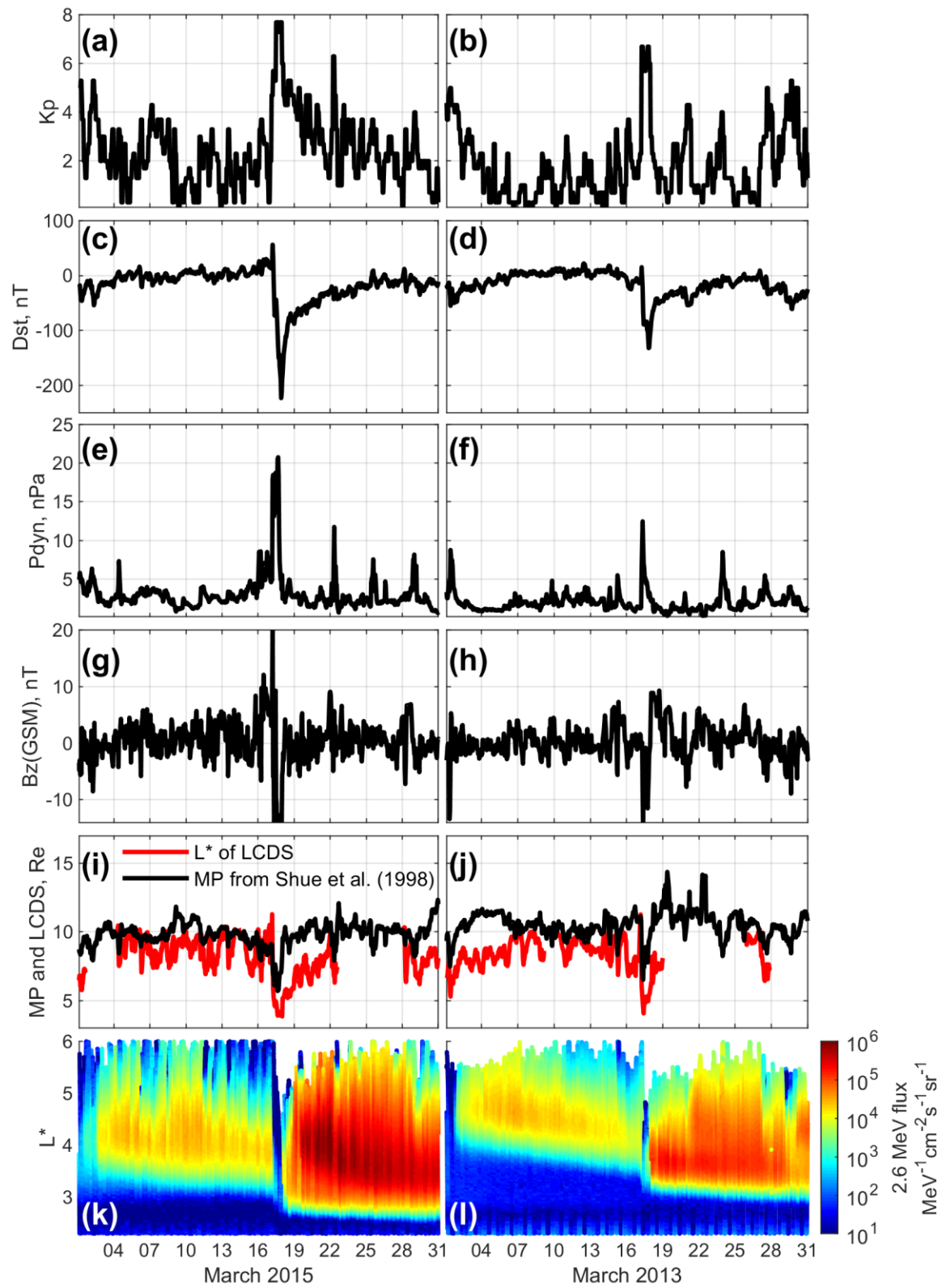
843 Usanova, M. E. et al. (2014), Effect of EMIC waves on relativistic and ultrarelativistic electron
844 populations: Ground-based and Van Allen Probes observations, *Geophys. Res. Lett.*,
845 41(5), 1375-1381, doi: 10.1002/2013GL059024.

Yu, Y., J. Koller, S. Zaharia, and V. Jordanova (2012), L* neural networks from different magnetic field models and their applicability, *Space Weather*, 10(2), doi: 10.1029/2011SW000743.

7 Acknowledgements

IRM is supported by a Discovery Grant from Canadian NSERC. This research was supported by funding from the Canadian Space Agency through a Geospace Observatory (GO) Canada Science and Applications grant. We acknowledge the WDC for Geomagnetism, Kyoto University, Japan for the geomagnetic indices (<http://wdc.kugi.kyoto-u.ac.jp/>). We also acknowledge use of NASA/GSFC's Space Physics Data Facility's OMNIWeb service, and OMNI data. CARISMA is operated by the University of Alberta, funded by the Canadian Space Agency (<http://omniweb.gsfc.nasa.gov/>). The authors thank D.K. Milling and the CARISMA team for the provision of data (<http://www.carisma.ca/>). Van Allen Probes ECT funding is provided by JHU/APL contract 967399 under NASA's Prime contract NAS5-01072 (https://rbsp-ect.lanl.gov/rbsp_ect.php). The GOES 13 and 15 magnetic field data are produced in real time by the NOAA Space Weather Prediction Center (SWPC) and are distributed by the NOAA National Geophysical Data Center (NGDC) (<http://satdat.ngdc.noaa.gov/sem/goes/data/>). Electron phase space density data used in this study is available from <https://drive.google.com/drive/u/0/folders/0ByNhSbWkAgdfaGt6TnJMcElhUTg>. A duplicate copy of the phase space density data is also available on the zenodo data repository <https://zenodo.org/record/3249418#.XTIQY-tKhEY>. The output from the plasmopause test

particle simulation used to specify the storm time location of the plasmapause is available from
http://enarc.space.swri.edu/PTP/. The LANLGeoMag software library is available
at https://www.github.com/drsteve/LANLGeoMag. LANL* neural network was used through
SpacePy python library (https://pythonhosted.org/SpacePy/). This research was enabled in part
by software provided by Compute Canada (http://www.computecanada.ca). All data used in the
paper is publicly accessible from the links provided above. All supporting material is available at
the zenodo data repository (see http://doi.org/10.5281/zenodo.3466079).



894 **Figure 1: Electron flux and selected geomagnetic and solar wind parameters during the**
895 **March 2015 (left) and March 2013 (right) storms. (a),(b) Geomagnetic index, Kp; (c),(d)**
896 **Geomagnetic activity index, Dst; (e),(f) Solar wind dynamic pressure measured at the L1**
897 **point; (g),(h) interplanetary magnetic field Bz component in geocentric solar**
898 **magnetospheric (GSM) coordinates measured at the L1 point; (i),(j) Magnetopause**
899 **location in (R_E), based on Shue et al. (1998) and the L^* (TS04D) location of the last closed**
900 **drift shell; (k),(l) electron flux at an energy of 2.6 MeV as a function of time and L^***
901 **(TS04D) measured by the Van Allen Probes.**

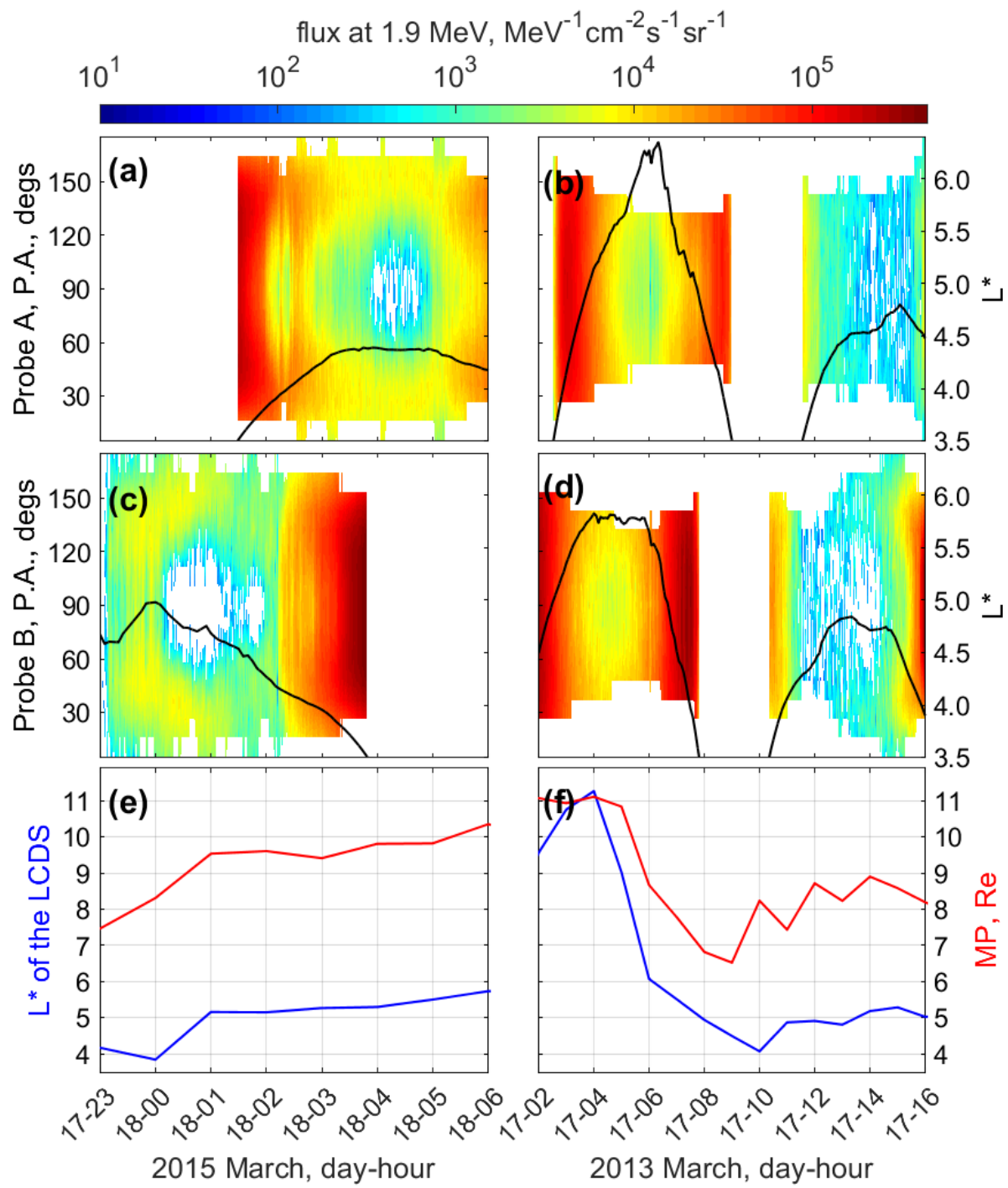


Figure 2: Panels (a) – (d) show the pitch angle, (P. A.) distributions of the electron flux at an energy of 1.9 MeV measured by Van Allen Probes A (top row) and B (middle row) during the March 2015 (left panels) and March 2013 (right panels) flux dropouts. Overplotted is the L^* location of the probes, illustrated by the black curves. The red curves in panels (e) and (f) show the location of the magnetopause (MP) standoff distance in R_E , derived using the Shue et al. (1998) model and the blue curves also show the L^* location of the last closed drift shell (LCDS). Similar results for 1.0 MeV energy electrons are shown in supporting material Figure S1.

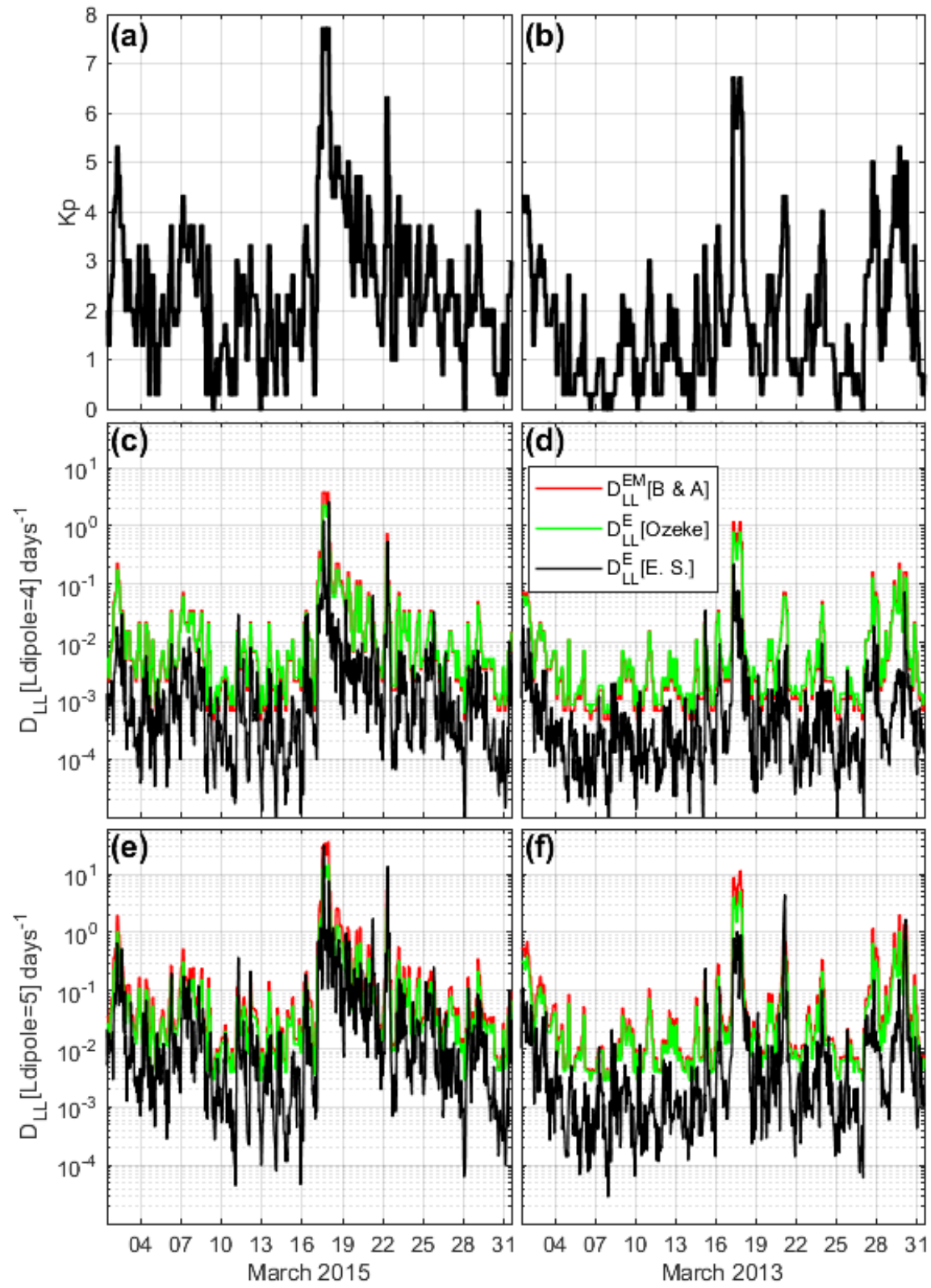
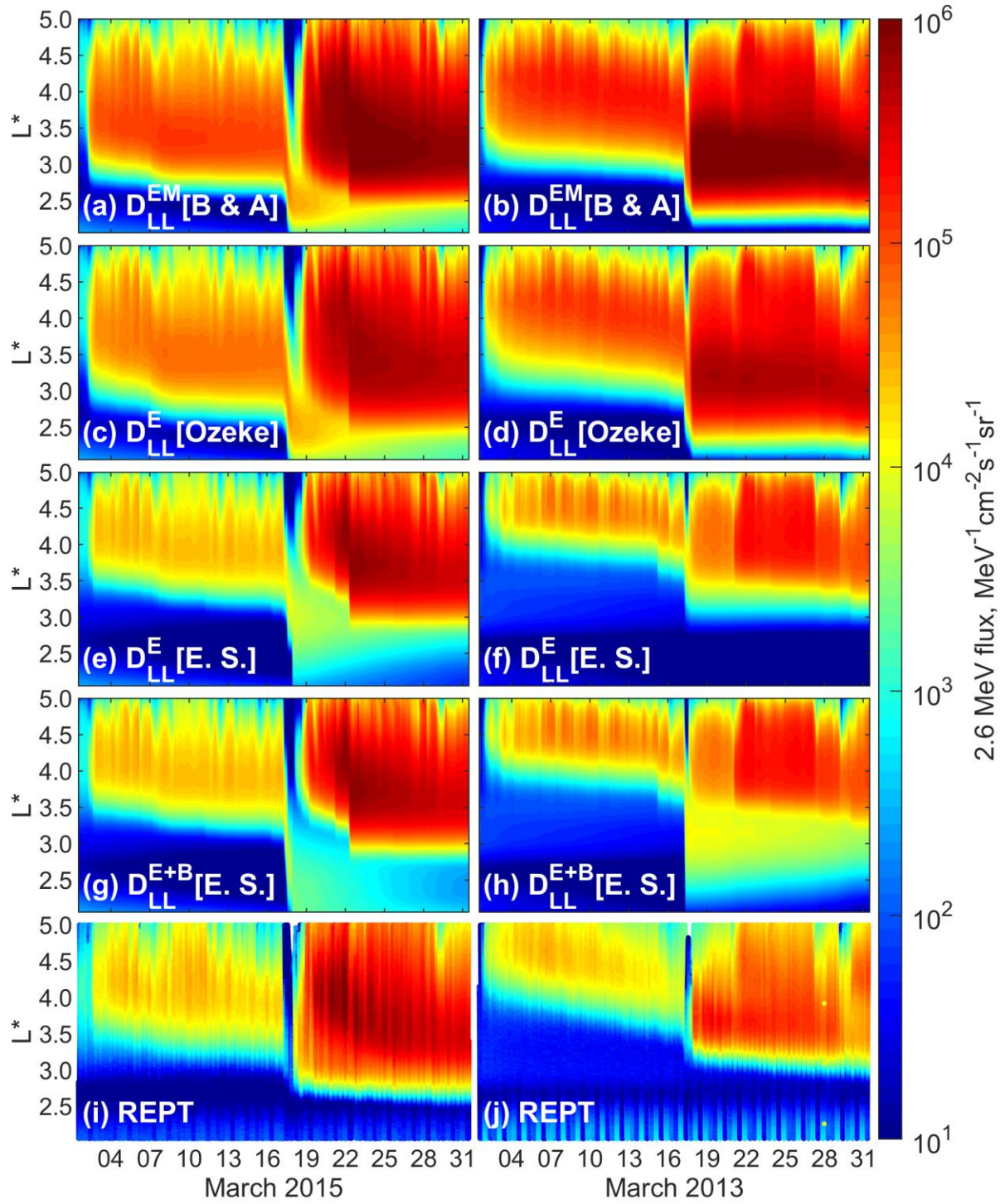


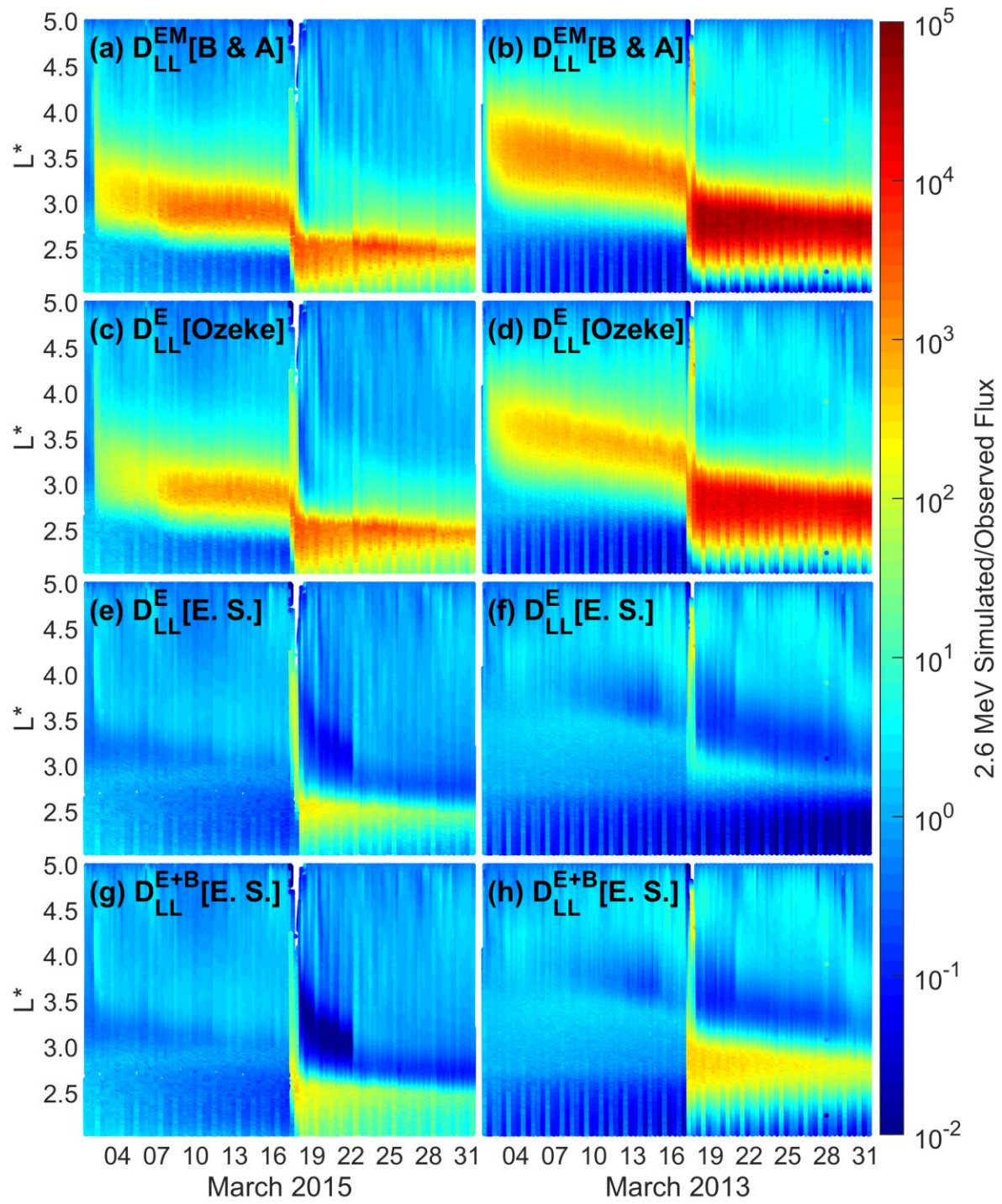
Figure 3: Radial diffusion coefficients at $L=4$ and $L=5$ during the March 2015 and March 2013 geomagnetic storms. Panels (a) and (b) show the Kp variation during the March 2015 (left column) and March 2013 (right column) storms, respectively. The radial diffusion coefficients as a function of Kp based on ULF wave statistics from Brautigam and Albert, (2000), D_{LL}^E [B & A], and Ozeke et al., (2014b), D_{LL}^E [Ozeke], are represented by the red and green curves, respectively. The event specific radial diffusion coefficients derived from ground-based magnetometer measurements, D_{LL}^E [E. S.] are represented by the black curves.



927
928
929

930

Figure 4: Comparison between the simulated and observed electron flux at an energy of 2.6 MeV as a function of L^* derived using the TS04D magnetic field model during the March 2015 (left) and March 2013 (right) storms derived using the radial diffusion coefficients presented in Figure 3. Panels (a) and (b) show the simulated electron flux derived using the electromagnetic radial diffusion coefficient formulism from Brautigam and Albert (2000), D_{LL}^{EM} [B & A]. Panels (c) and (d) show the simulated electron flux derived using the electric field radial diffusion coefficients from Ozeke et al. (2014b), D_{LL}^E [Ozeke]. Panels (e) and (f) show the simulated electron flux derived using event-specific electric field radial diffusion coefficients derived using ground-based magnetometer data, D_{LL}^E [E. S.]. Panels (g) and (h) show the simulated electron flux derived using D_{LL}^E [E. S.] with D_{LL}^E [E. S.] increased by a factor of 10 during the flux dropout interval representing enhanced storm time diffusion due to the compressional magnetic field D_{LL}^B [E. S.], consistent with the results presented in Olifer et al. (2019). Finally, panels (i) and (j) show the electron flux at an energy of 2.6 MeV as measured by the REPT instrument on-board the Van Allen Probes.



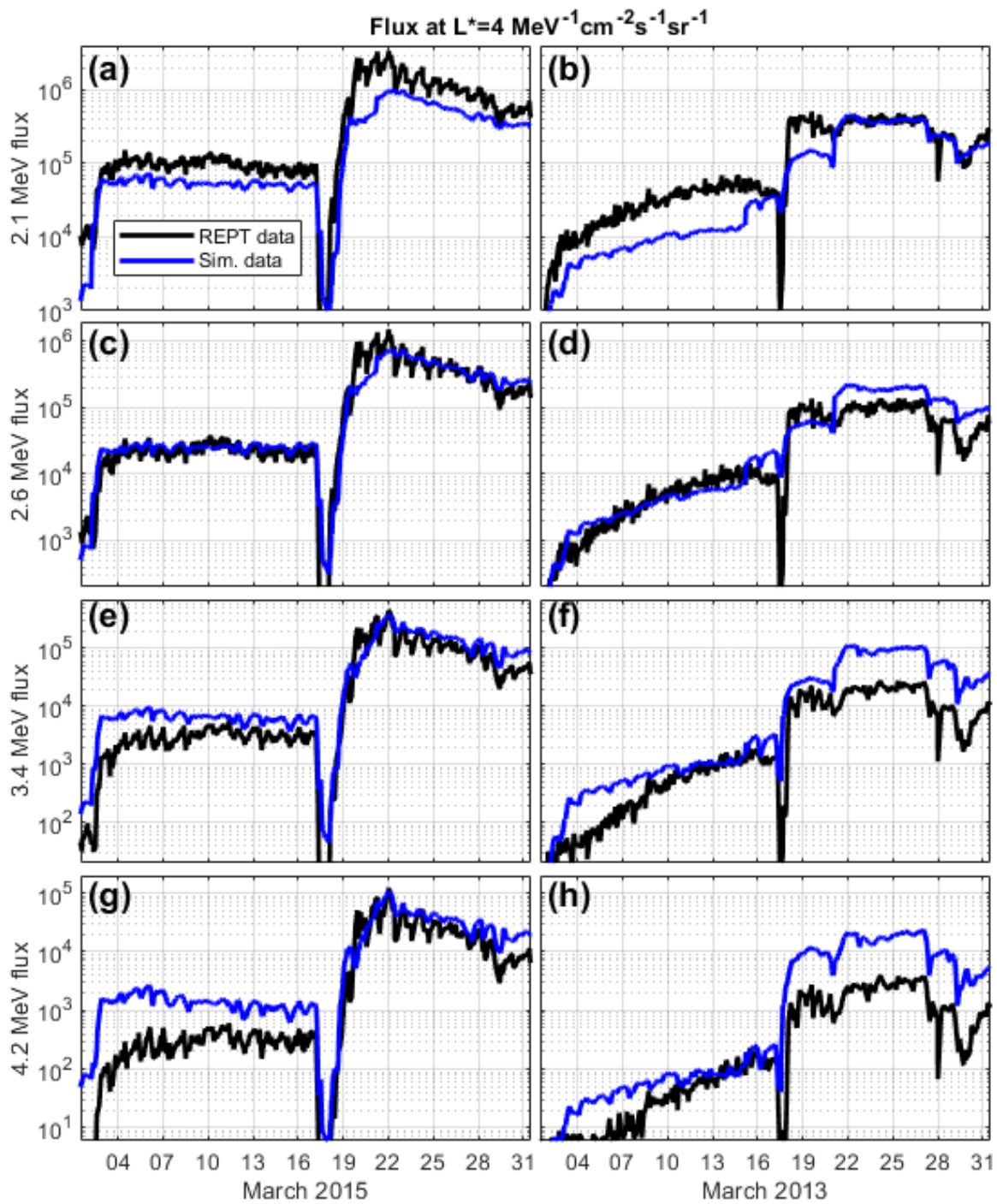
947

948

949

950

951 **Figure 5: The ratio of the simulated over the observed electron flux values presented in**
952 **Figure 4 during the March 2015 (left) and March 2013 (right) magnetic storms. Red to**
953 **yellow regions indicate L-shells and times where the simulated flux is much greater than**
954 **the observed flux. Similarly, the dark blue regions indicate regions where the simulated**
955 **flux is lower than the observed flux.**

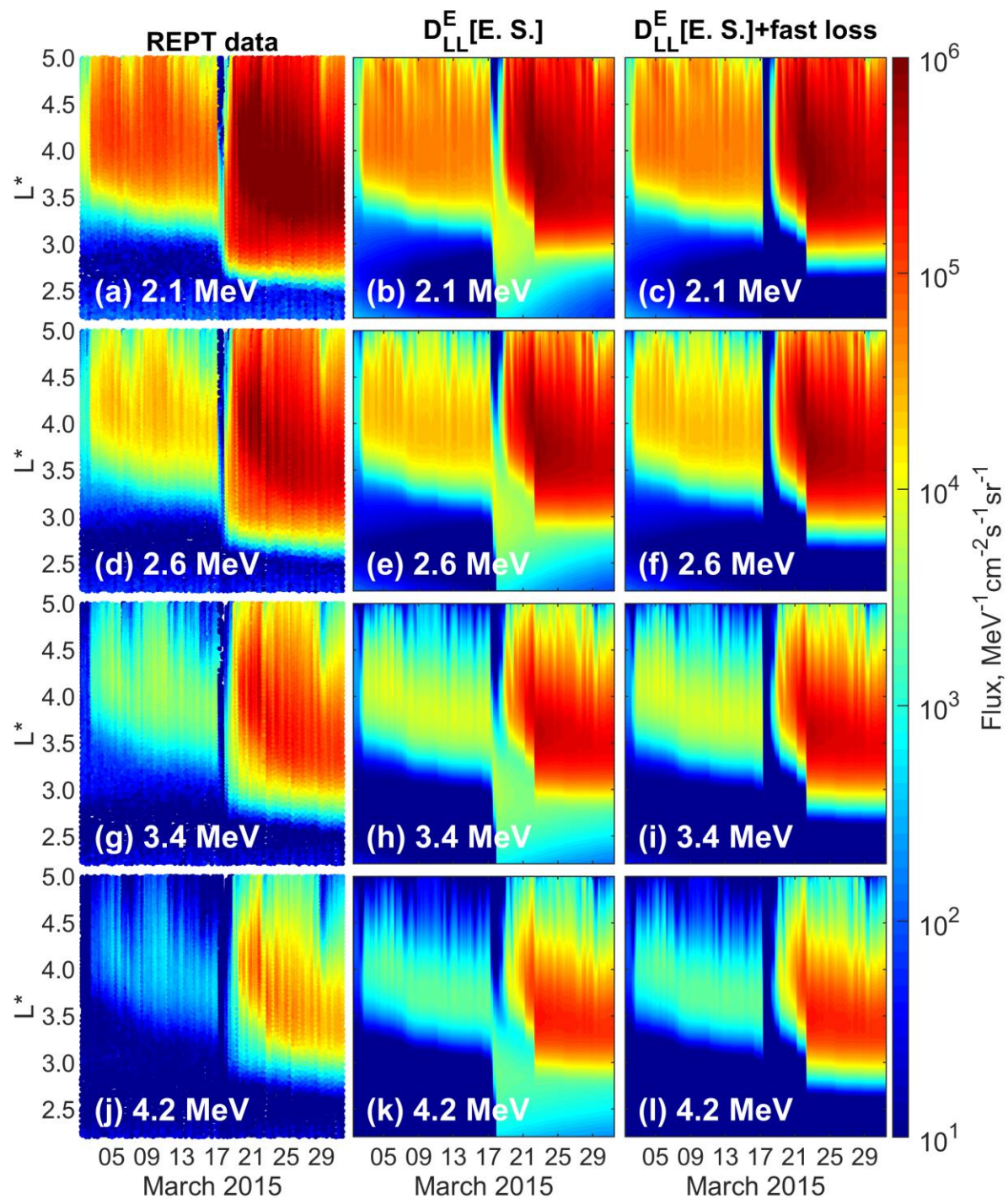


956

957

958

Figure 6: Comparison between the observed, (black curve), and simulated, (blue curve), electron flux at $L^*=4$ and at energies of 2.1, 2.6, 3.4 and 4.2 MeV during the March 2015 (left) and March 2013 (right) magnetic storms. During both the March 2013 and 2015 storms, at fixed $L^*=4$, the simulated (blue curve) and measured (black curves) ultra-relativistic electron flux values are in good agreement with each other to within an order of magnitude at all energies from 2.1 MeV to 4.2 MeV



970

971

972

Figure 7: Comparison between the observed and simulated electron flux at energies of 2.1, 2.6, 3.4 and 4.2 MeV as a function of L^* using the TS04D magnetic field model during the March 2015 storm. Panels (a), (d), (g), and (j) (left column) show the observed flux. Panels (b), (e), (h), and (k) (middle column) show the simulated electron flux using radial diffusion coefficients obtained from global ground magnetometer measurements of the ULF wave power, D_{LL}^E [E. S.]. Panels (c), (f), (i), and (l) (right column) show the simulated electron flux again using D_{LL}^E [E. S.] but with a short time interval of artificial loss with $\tau=1$ hour included at $L^*<3.5$, presenting additional fast loss.

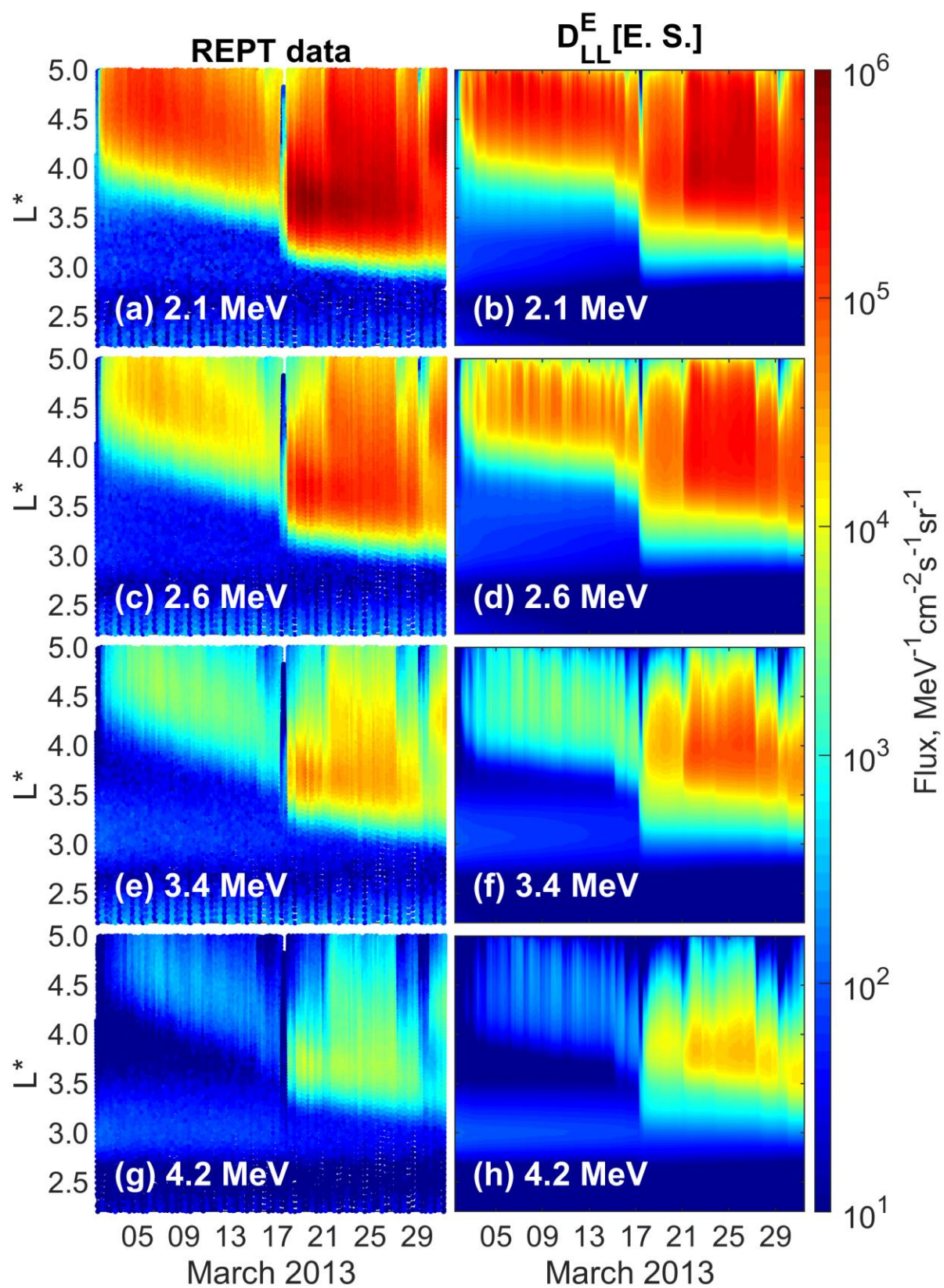
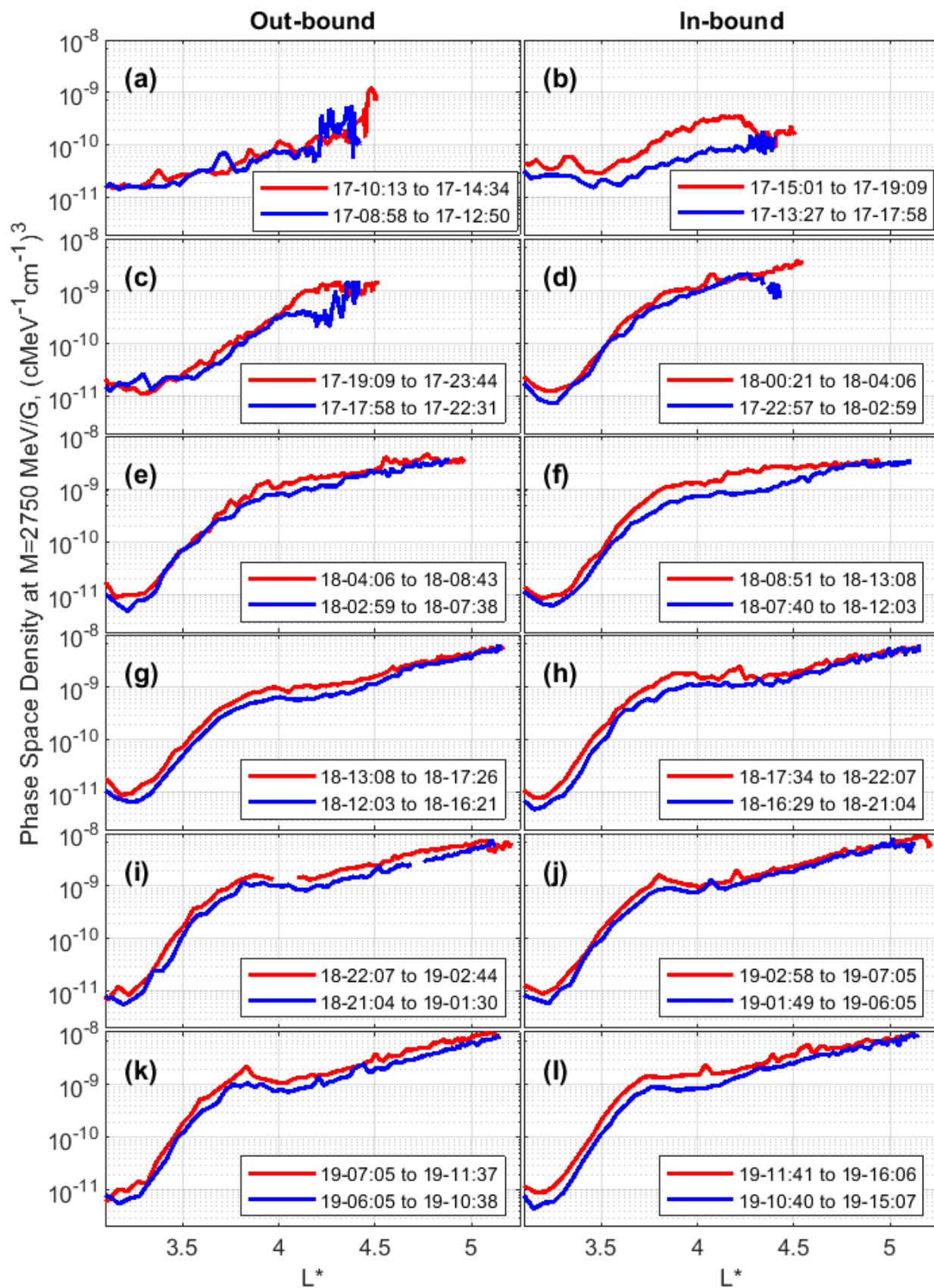


Figure 8: Comparison between the observed and simulated electron flux at energies of 2.1, 2.6, 3.4 and 4.2 MeV as a function of L^* using the TS04D magnetic field model during the March 2013 storm. Panels (a), (c), (e), and (g), (left columns) show the observed flux. Panels (b), (d), (f), and (h), (right columns) show the simulated electron flux using radial diffusion coefficients obtained from global ground magnetometer measurements of the ULF wave power, D_{LL}^E [E. S.]. As described in the text, the flux at the outer boundary at, $L^*=5$, is set to zero on March 17 from 8 UT to 24 UT. No additional artificial fast losses are included, see text for details.



995 **Figure 9: Evolution of the electron phase space density profiles as a function of L^* at**
996 **$M=2750$ MeV/G and $K=0.17$ G^{1/2}Re during the March 2013 storm. The red and blue curves**
997 **represent phase space density profiles derived from Van Allan Probes A and B,**
998 **respectively. The start and end times of the out and in bound passes are shown in the**
999 **legend in the format day-hour:minute. Similar plots for $M=1590$ MeV/G and $M=3980$**
1000 **MeV/G electrons are shown in the supporting material in Figure S5 and Figure S6,**
1001 **respectively.**
1002



[Journal of Geophysical Research-Space]

Supporting Information for

**Rapid Outer Radiation Belt Flux Dropouts and Fast
Acceleration during the March 2015 and 2013 Storms: The
Role of ULF Wave Transport from a Dynamic Outer
Boundary**

**L. G. Ozeke¹, I. R. Mann¹, S. K. Y. Dufresne¹, L. Olifer¹, S. K. Morley², S. G.
Claudepierre^{3,4}, K. R. Murphy⁵, H. E. Spence⁶, D. N. Baker⁷ and A. W. Degeling⁸**

¹Department of Physics, University of Alberta, Edmonton, Alberta, Canada

²Los Alamos National Laboratory, Los Alamos, New Mexico, USA

³Space Sciences Department, The Aerospace Corporation, Los Angeles, California, USA

⁴Department of Atmospheric and Oceanic Sciences, University of California, Los Angeles, CA, USA

⁵NASA Goddard Spaceflight Center, Code 674, Greenbelt, Maryland, MD 20771, USA

⁶Institute for the Study of Earth, Oceans, and Space, University of New Hampshire, Durham, New Hampshire, USA

⁷Laboratory for Atmospheric and Space Physics, University of Colorado Boulder, Boulder, Colorado, USA

⁸Institute of Space Science, Shandong University, Weihai, China

Correspondence to: L. G. Ozeke (lozeke@ualberta.ca)

Contents of this file

Supporting Figures S1, S2, S3, S4, S5 and S6, including a brief explanation of their content as a supplement to the results and conclusions drawn in the main article.

Introduction

Results showing the pitch-angle distribution during the March 2015 and March 2013 flux dropout intervals in the same format as Figure 2 in the main article except for 1.0 MeV energy electrons instead of for 1.9 MeV energy electrons, are presented in supporting Figure S1. Figure S2 shows the time interval where the last closed drift (LCDS) drops below $L^*=5$ during the March 2015 and 2013 storms, indicating that at these times electrons at $L^*>5$ would be lost to the magnetopause. The results presented in Figure S2 are used to specify the times where the outer boundary condition at $L^*=5$ in the simulation results presented in the main article are set to zero. Figure S3 shows the location of the plasmopause used to separate the regions where plasmaspheric hiss loss and chorus loss are applied in the simulations presented in the main article. Figure S4 is the same as Figure 4 in the main article except during the flux dropout interval the outer boundary where the flux is set to zero is moved inward to $L^*=4$. Figures S5 and S6 show the evolution of the electron phase space density in the same format and at the same K-value as shown in Figure 9 in the main article except at first adiabatic invariants of 1590 MeV/G and 3980 MeV/G instead of 2750 MeV/G.

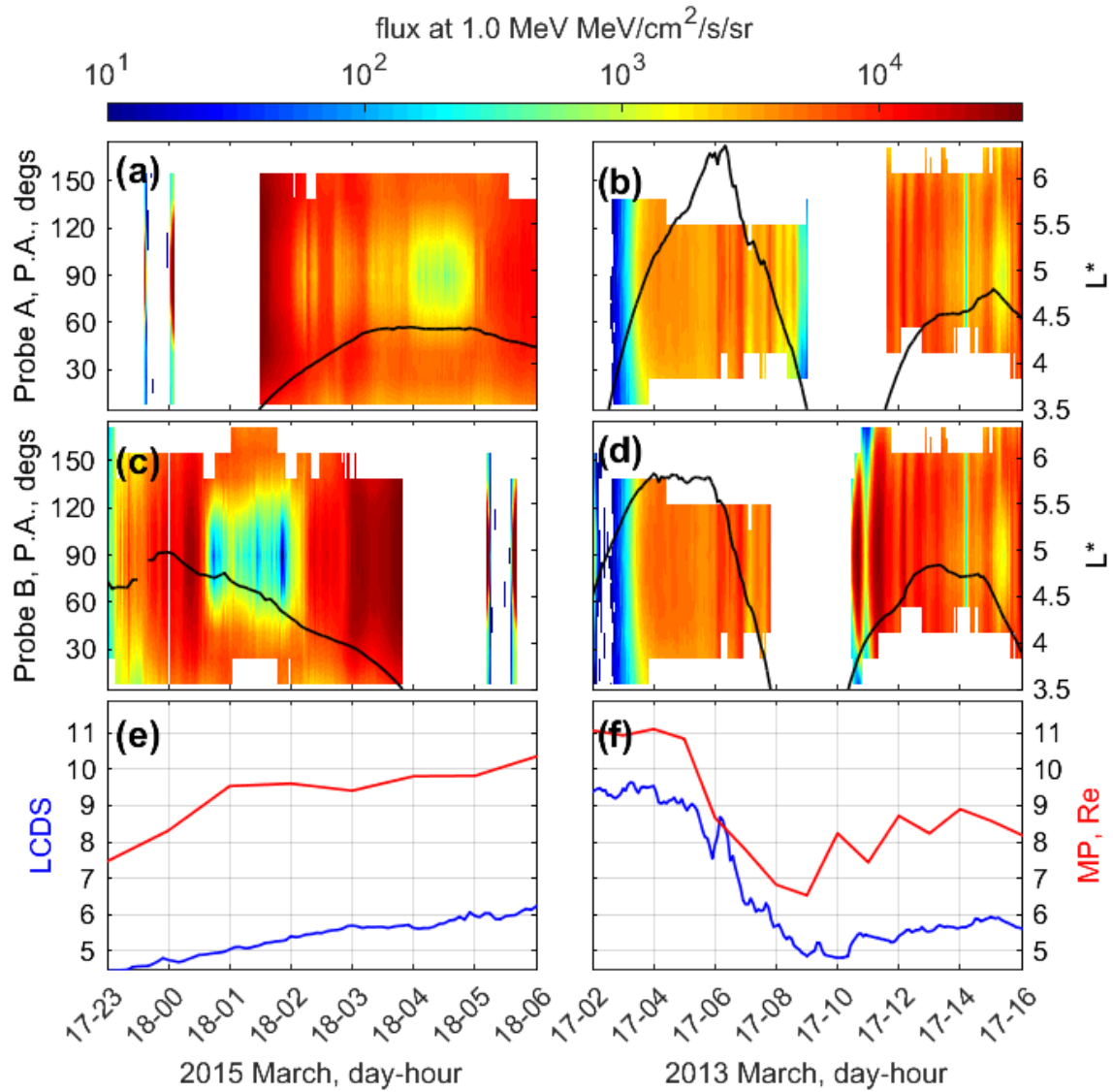


Figure S1: Panels (a) – (d) show the pitch angle, P. A. distributions of the 1.0 MeV electron flux measured by the Van Allen Probes during the March 2015 (left panels) and March 2013 (right panels) flux dropouts. The red curves in panels (e) and (f) show the location of the magnetopause MP, derived using the Shue et al. (1998) model, the blue curves show the location of the last close drift shell LCDS.

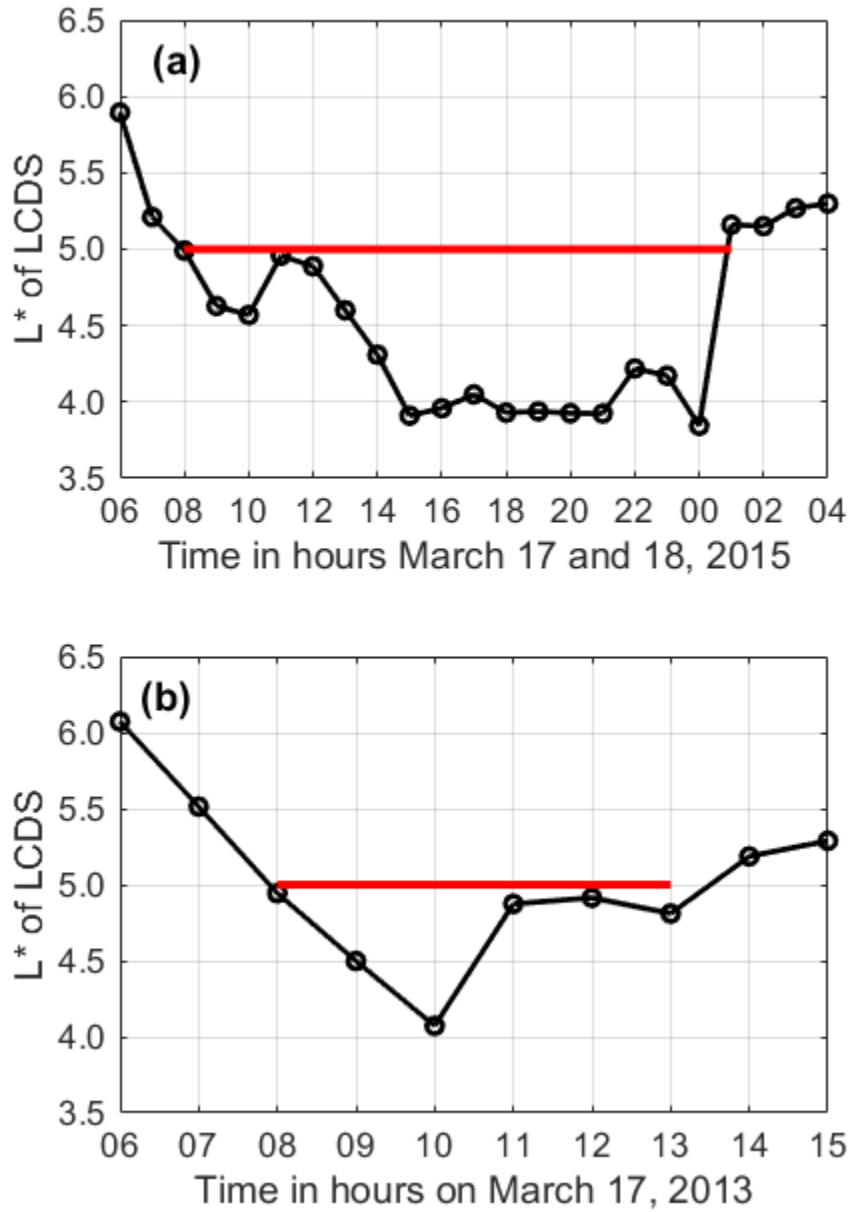


Figure S2: Hourly averaged L^* values of the last closed drift shells (LCDS) during the March 2015 (a) and March 2013 (b) geomagnetic storms. The LCDS was derived at $K=0.05 \text{ G}^{1/2}\text{Re}$ using the TS04 Tsyganenko and Sitnov (2005) model and the LANLGeoMag software library (Henderson et al., 2017). The time intervals highlighted in red indicates the times where the LCDS dropped below L^* of 5, the location of the outer boundary condition used for the simulations presented Figures 4, 5, 6, 7 and 8 in the main article. At these times the outer boundary condition used in the simulations was set to zero, representing electron loss to the magnetopause.

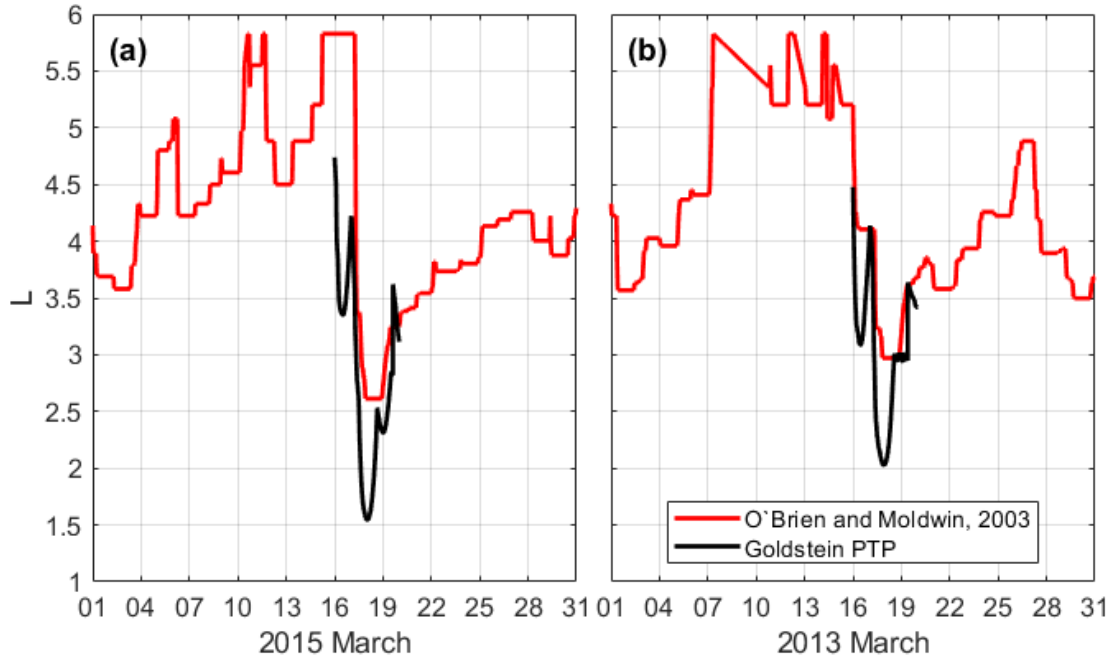


Figure S3: L-shell location of the plasmapause during the March 2015 (a) and March 2013 (b) storms derived using the empirical O'Brien and Moldwin (2003) model as a function of the Dst index and the plasmapause test particle (PTP) simulation output presented in Goldstein et al. (2014a, 2014b).

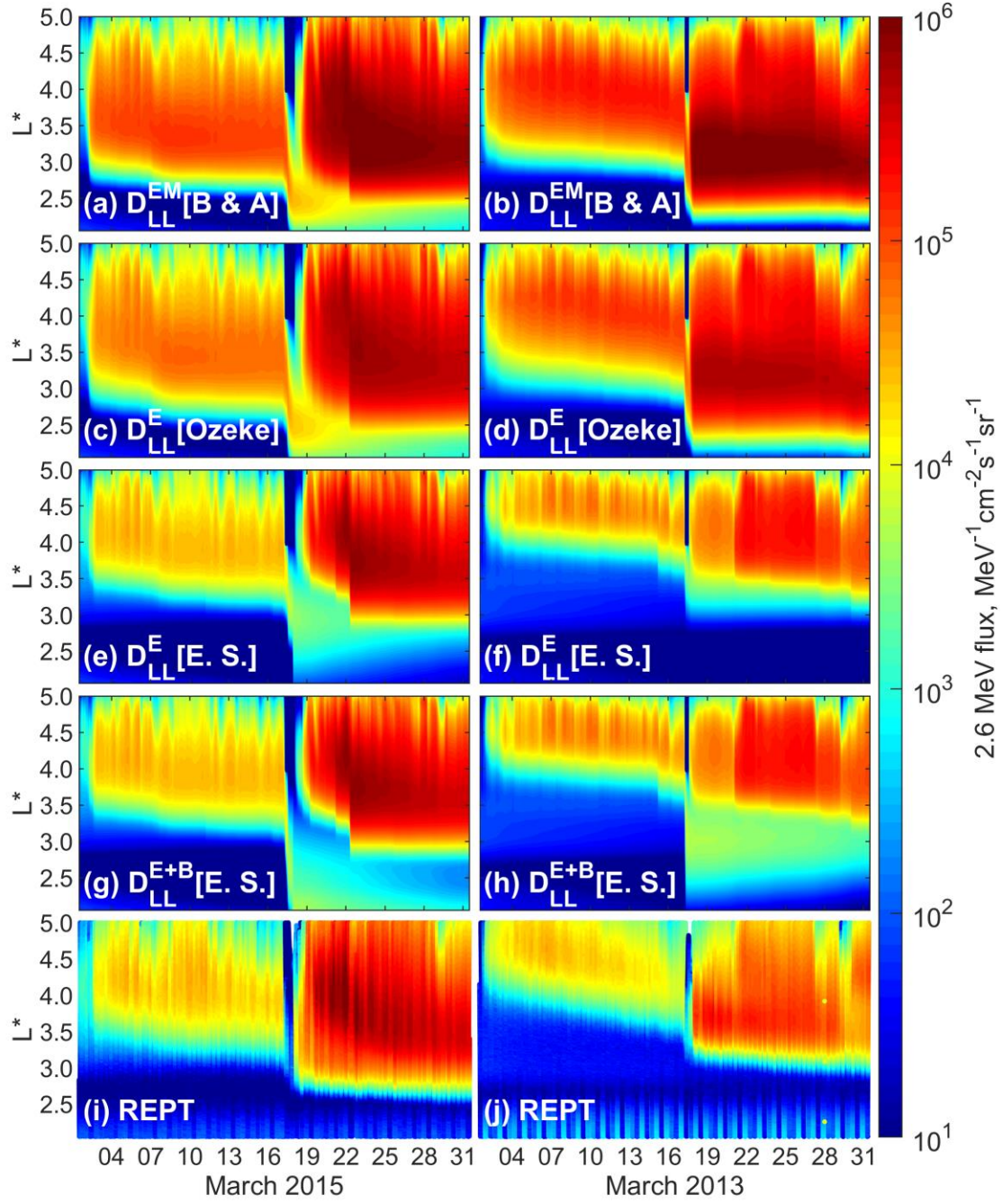


Figure S4: Comparison between the simulated and observed electron flux in the same format as Figure 4 in the main article. Here the during the dropout intervals the electron flux is set to zero at all energies and L-shells down to $L^*=4$.

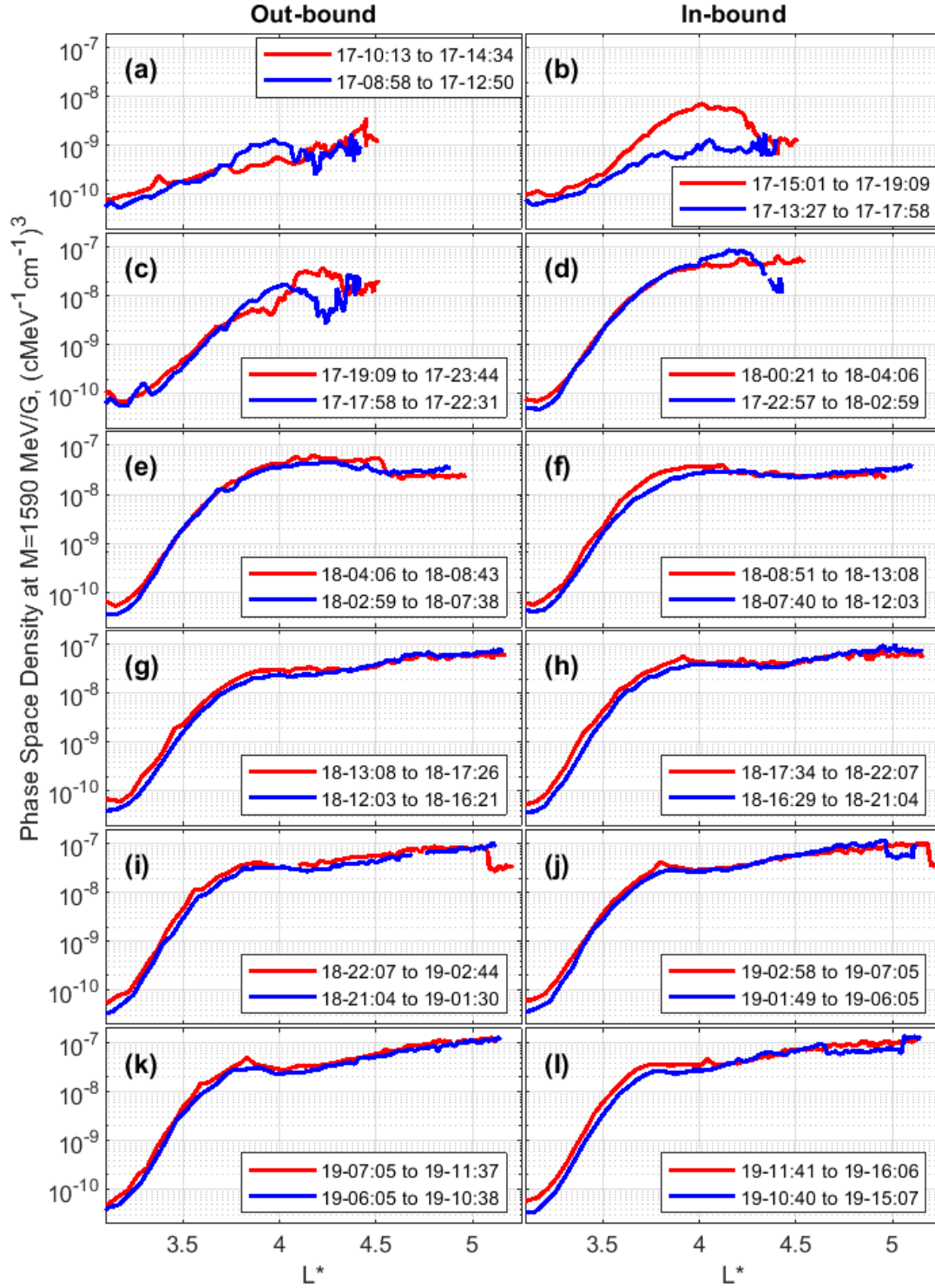


Figure S5: Evolution of the electron phase space density profiles at $M=1590$ MeV/G and $K=0.17$ $G^{1/2}Re$ during the March 2013 storm. The red and blue curves represent PSD profiles derived from Van Allan Probes A and B. The start and end times of the out and in bound passes are shown in the legend in the format day-hour:minute.

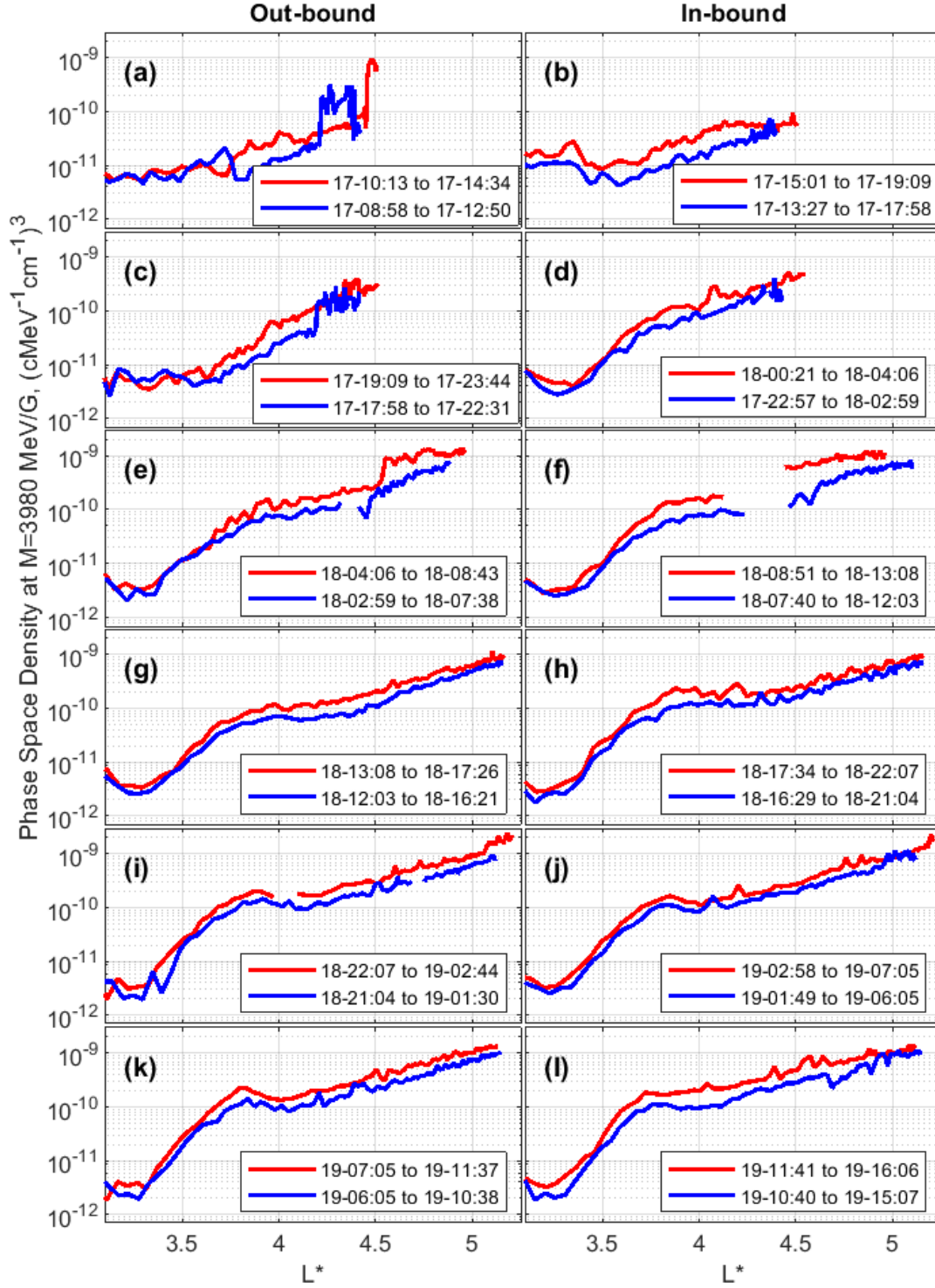


Figure S6: Evolution of the electron phase space density profiles at $M=3980$ MeV/G and $K=0.17$ $G^{1/2}Re$ during the March 2013 storm. The red and blue curves represent PSD profiles derived from Van Allan Probes A and B. The start and end times of the out and in bound passes are shown in the legend in the format day-hour:minute.